Eur. Phys. J. B (2025)98:160
https://doi.org/10.1140/epjb/s10051-025-01004-2

THE EUROPEAN PHYSICAL JOURNAL B

Research - Condensed Matter

Boosting the photocatalytic hydrogen production via the S/Zr co-doping in a $CaTiO_3$ perovskite: first-principles study of the optoelectronic, thermodynamic, and photocatalytic

Abdellah Bouzaid[1,2,a], Younes Ziat[1,2], Hamza Belkhanchi[1,2,b], and Hmad Fatihi[3]

[1] Engineering and Applied Physics Team (EAPT), Superior School of Technology, Sultan Moulay Slimane University, Beni Mellal, Morocco
[2] The Moroccan Association of Sciences and Techniques for Sustainable Development (MASTSD), Beni Mellal, Morocco
[3] Laboratory of Research in Physics and Engineering Sciences, Polydisciplinary Faculty, Sultan Moulay Slimane University, Beni Mellal, Morocco

Received 16 May 2025 / Accepted 15 July 2025

Abstract. Recent advancements in photocatalysis research have mostly concentrated on the development of effective materials to enhance water splitting and the production of hydrogen. This work used density functional theory (DFT) to investigate the structural, optoelectronic, thermodynamic characteristics, and redox band edges of undoped and (S, Zr) co-doped $CaTiO_3$. The initial structural optimization results indicate that undoped and (S, Zr) co-doped $CaTiO_3$ have negative formation energies, signifying their thermodynamic stability. Furthermore, thermodynamic analysis indicates a significant change in the Grüneisen parameter, Debye temperature, entropy, and heat capacities due to co-doping, showing the change of lattice anharmonicity and vibrational characteristics with variations in temperature and pressure. Optoelectronic calculations show that undoped $CaTiO_3$ has an indirect band gap of 2.77 eV. In contrast, co-doping with S and Zr results in direct band gaps of 2.22 eV for $Ca_8Ti_7Zr_1O_{23}S_1$ and 1.85 eV for $Ca_8Ti_6Zr_2O_{22}S_2$, which reduces the band gap and enhances visible light absorption and optical conductivity. Furthermore, the analysis of the valence and conduction band edge positions (E_{VB} and E_{CB}) of Zr- and S-co-doped $CaTiO_3$ indicates that the material satisfies the thermodynamic requirements for water splitting, underscoring its potential as an efficient photocatalyst. Notably, the observed variations in electronic and thermodynamic properties with increasing dopant concentration reveal a nonlinear trend, suggesting a complex interplay between dopant interactions and host lattice distortions. These findings suggest that co-doped materials exhibit promising properties for renewable energy applications, particularly solar-driven photocatalytic hydrogen production, photovoltaic devices, and optoelectronics, due to their enhanced visible light absorption.

1 Introduction

The development of renewable energy solutions represents a major strategic challenge in view of today's economic and environmental challenges. Among these solutions, renewable energy sources, notably photovoltaic (PV) systems, wind power and battery storage technologies, offer promising prospects for meeting growing energy demand while reducing environmental impact [1–4]. Abundant, clean solar energy is an attractive alternative, as it generates no greenhouse gas emissions [5, 6]. Since Fujishima and Honda's seminal 1972 discovery demonstrating hydrogen production via TiO_2 under UV irradiation, significant advances have been made in the field of photocatalytic materials [7]. However, a major limitation of TiO_2 is its high band gap, restricting its absorption to less than 4% of the solar spectrum [8, 9]. Those technologies have been crucial for boosting the energy security, reducing the greenhouse gas emissions and stimulating the long-term economic development [10]. To ensure the optimal environmental sustainability and energy resilience, innovation and integration of the renewable energies into the existing infrastructures have been essential, particularly through the optimization of photocatalytic materials [11]. Among those advances, molecular hydrogen (H_2) has stood out as a clean and efficient energy carrier, generating no pollutants or greenhouse gases when used, and boasting a

[a] e-mail: abdellah.bouzaid97@gmail.com
[b] e-mail: hamzastudentestbm@gmail.com (corresponding author)

Published online: 31 July 2025

high specific energy (122 kJ/g) [12]. Green hydrogen production has been particularly attractive because it has released only water (H_2O) as a by-product, thus eliminating the carbon dioxide (CO_2) emissions [13, 14]. As a result, green hydrogen has played a key role in the transition to the sustainable energy systems [13, 15]. Density functional theory (DFT) is a robust tool for exploring the quantum–mechanical properties of materials in diverse applications [16–19]. In the past year, semiconductor perovskite materials have garnered increasing interest as potential candidates for applications in catalysis, photovoltaics, electronics, and optoelectronics, due to their exceptional optical characteristics and structural adaptability [20–24]. Moreover, Hasan et al. [25] used first-principles calculations to examine the structural, mechanical, thermodynamic, electronic, and optical properties of ABO_3 perovskites (A = Ba, Ca, Sr; B = Ce, Ti, Zr). Their findings indicated the stability, favorable mechanical behavior, and promising electronic and thermal properties of these compounds, suggesting their potential for optoelectronic, photonic, and thermoelectric applications. Furthermore, perovskite oxides (ABO_3) are emerging as particularly promising materials for water dissociation photocatalysis and hydrogen production (HP) due to their excellent photocatalytic (PC) properties [26–29]. However, pure $CaTiO_3$, despite its potential, has a wide band gap (3.5 eV), limiting its efficiency under visible light and resulting in moderate photocatalytic activity for hydrogen evolution [30]. Several strategies have been proposed to reduce the band gap of perovskite materials and improve their activity under visible light. Among them, doping with foreign elements is a simple and effective approach [31]. Recently, doping $CaTiO_3$ with (La-S) at a ratio of 0.25 led to a significant improvement in water dissociation photocatalysis thanks to a reduced bandgap, enhanced visible light absorption, and improved electron mobility [32]. Yang et al. [33] demonstrated that cubic $SrTiO_3$ exhibits superior toluene degradation efficiency (80%) compared to tetragonal $CaTiO_3$ (20%) due to its enhanced ROS production, O_2/H_2O adsorption, and selectivity for benzoic acid. Theoretical calculations corroborated these findings, emphasizing the crucial influence of crystal structure on photocatalytic activity. Furthermore, theoretical studies based on density functional theory (DFT) have explored various dopings to optimize these materials. Attou et al. have shown that doping $CaTiO_3$ with boron (B) at the oxygen sites lowers the band gap and improves reactivity under visible light, thanks to the introduction of additional p-energy levels [34]. Furthermore, Zhang et al. demonstrated by DFT calculations that the enhancement of visible light absorption in copper-doped $CaTiO_3$ is mainly due to Cu^{2+-}induced electronic transitions [35]. Furthermore, the study of co-doped $CaTiO_3$ (Zn, Pr) reveals structural modifications similar to those of Pr mono-doped, but the addition of Zn leads to the formation of localized gap states due to hybridization of the Pr 4f, O 2p, and Ti 3 d orbitals [36]. Zulfiqar et al. [37] demonstrate that co-doping $BaTiO_3$ with zirconium (Zr) and chalcogen elements, specifically sulfur (S), selenium (Se), and tellurium (Te), enhances the stability of the dopants, generates direct band gaps, and increases visible light absorption. This positions Zr- and Te-co-doped $BaTiO_3$ as a promising candidate for photocatalytic hydrogen production. Furthermore, Zulfiqar et al. [38] demonstrate that co-doping $BaZrO_3$ with Ti and chalcogens (S, Se, Te) reduces the band gap and enhances visible light absorption. Their DFT calculations identify Ti and Te co-doped $BaZrO_3$ as a stable and highly promising material for solar water splitting due to its improved light absorption. Similar studies on other doped perovskite oxides show that nitrogen doping in $SrTiO_3$ introduces impurity states, enhancing visible light absorption and reducing the band gap to 2.03 eV, which improves photosensitivity and charge carrier transport. DFT calculations confirm that these modifications promote efficient electron–hole separation, making N-doped $SrTiO_3$ a promising photocatalyst for solar water splitting [39]. However, Alves et al. [40] examined the influence of S, Se, and Te doping on $NaTaO_3$, revealing a notable red shift in the absorption edge, diminished band gaps, and enhanced photocatalytic efficacy under visible light, especially in Te-doped configurations attributed to improved charge separation and carrier mobility. Similar, Mouhib et al. [41] found that doping $ATiO_3$ (A = Ca, Sr, Ba) with S, Se, or Te at oxygen sites gradually reduced the bandgap while preserving p-type semiconducting behavior. Te-doped $BaTiO_3$ exhibited enhanced visible light absorption, suggesting its potential for photovoltaic applications. Another study used first-principles calculations to study the structural, optoelectronic, mechanical, and photocatalytic properties of hydrogen-doped $CsSrO_{3-x}H_x$. The findings demonstrated that structural distortions, bandgap narrowing, and a change from an indirect to a direct bandgap were caused by an increase in hydrogen content. The most effective composition for photocatalytic applications was found to be $CsSrO_{2.4}H_{0.6}$, and the compound remained stable with favorable redox potentials for water splitting [42]. Ou-Khouya et al. [43] showed that doping S, Se, and Te in $SrTiO_3$ improves optical conductivity, dielectric constant, and visible light absorption while dramatically decreasing the bandgap with increasing dopant concentration. Te-doped $SrTiO_3$ performed the best among the doped systems, making it a viable option for solar cell and photovoltaic applications. Similar results have been observed with other doping combinations. Yan et al. demonstrated that in Zr-doped TiO_2, hybridization of the O $2p$ and S $3p$ orbitals alters energy levels near the valence band (VB), while the Zr 4 d orbital separates the O $2p$ and Ti $3d$ states in the conduction band (CB), thus reducing electron–hole recombination [44]. Furthermore, the distance between the S and Zr atoms strongly influences the electronic and optical properties, generating a red shift in the absorption edge of co-doped TiO_2 [44]. Furthermore, recent studies have shown that (Zr, S), (Zr, Se), and (Zr, Te) co-dopings

lead to a narrowing of the bandgap and an enhancement of photoactivity under visible light in the TiO_2 monolayer (111). Notably, Te-doped and co-doped (Zr, Te) monolayers are shown to be the most efficient photocatalysts for hydrogen production [45].

Although doped perovskite materials have attracted considerable attention, to the best of our knowledge, no systematic experimental or theoretical investigation on the electronic structure, optical properties, and photocatalytic performance of S/Zr co-doped $CaTiO_3$ under visible light irradiation for hydrogen production has been conducted. Moreover, co-doped perovskite materials is an effective strategy to optimize their electronic and optical properties for enhanced photocatalysis. Specifically, sulfur (S) and zirconium (Zr) co-doped of $CaTiO_3$ can synergistically improve light absorption, and catalytic efficiency. Using density functional theory (DFT) calculations, we investigated the structural, thermodynamic, electronic, and optical properties of S and Zr co-doped $CaTiO_3$ using a $2 \times 2 \times 2$ supercell. Computed formation energies confirm the thermodynamic stability of the co-doped structures. Our analysis reveals significant bandgap narrowing, enhanced visible light absorption, and favorable band edge alignment for water redox potentials. According to these results, S/Zr co-doped $CaTiO_3$ shows promising properties for renewable energy applications, especially in solar-driven photocatalytic hydrogen production, photovoltaic, and optoelectronic devices, because of its improved electronic properties and enhanced visible light response.

2 Computational details

The structural, optoelectronic, and photocatalytic properties of undoped and (S, Zr) co-doped perovskite materials were investigated using DFT [46] within the full potential linearized augmented plane wave (FP-LAPW) framework implemented in the WIEN2K code [47]. Volume optimization and structural relaxation were conducted using the generalized gradient approximation (GGA) functional [48], while the modified Becke–Johnson potential (TB-mBJ) was employed, which has been consistently shown to yield results in close agreement with experimental data [49]. Convergence was ensured by setting $R_{\mathrm{MT}}{}^{*}K_{\max} = 7$, with Muffin-tin radii of (2.5, 1.92, 1.74) for $CaTiO_3$, (2.50, 1.92, 1.92, 1.74, 1.74) for $Ca_8Ti_7Zr_1O_{23}S_1$, and $Ca_8Ti_6Zr_2O_{22}S_2$. A k-points range of 1000 was used for undoped $CaTiO_3$, while co-doped systems employed 500 k-points for structural optimization and 1000 k-points for optoelectronic properties. The findings were acquired using a convergence criterion of 10^{-5} Ry for energy and 10^{-4} e for charge. The in-depth study of electronic densities of states, band structures, and dielectric functions enabled us to assess the impact of co-doping on the optical response of the material. In addition, analysis of thermodynamic properties, notably formation energies and phase stability, revealed an improvement in the stability of doped $CaTiO_3$, suggesting its suitability for practical applications in photocatalysis. These discoveries elucidate the underlying principles regulating the behavior of perovskite materials and facilitate their optimization for renewable energy applications, especially in photocatalysis and optoelectronic devices.

3 Results and discussion

3.1 Structural properties

The perovskite oxide $CaTiO_3$ crystallizes in a cubic structure, belonging to the Pm-3m space group (no. 221), which is characteristic of perovskite-type materials. This structure features high symmetry and well-defined atomic organization. In the unit cell (shown in Fig. 1a), Ca atoms occupy the corner sites with coordinates (0, 0, 0), while the titanium (Ti) atom is positioned in the center of the mesh at coordinates (0.5, 0.5, 0.5). Oxygen atoms (O) are located in positions centered on the faces, at coordinates (0.5, 0.5, 0). This atomic arrangement gives $CaTiO_3$ high structural stability, making it a promising material for numerous technological applications, notably in optoelectronics and photocatalysis.

To study the effects of co-doping, a $2 \times 2 \times 2$ supercell of undoped cubic $CaTiO_3$ was constructed. This supercell, composed of 40 atoms, includes 8 Ca atoms, 8 Ti atoms, and 24 O atoms. To assess the influence of doping elements, we analyzed two distinct scenarios: firstly the individual incorporation of S and Zr enabled us to examine their respective effects on the structure and electronic properties of the material. Then a second type of co-doping was studied by simultaneously introducing two atoms of S and two atoms of Zr.

Zr was substituted at Ti sites, while the introduction of S at oxygen sites maintained charge balance in the co-doped systems, in accordance with the electronic equilibrium relation $Ti^{4+} + O^{2-} = Zr^{4+} + S^{2-}$. The simultaneous addition of these two elements aims to modulate the electronic and optical properties of $CaTiO_3$, seeking an optimal compromise between bandgap broadening and enhanced absorption capabilities in the visible range. The electronic configurations of the elements involved in the calculations were as follows: Ca: $4s^2$, O: $2s^2 2p^4$, Ti: $3d^2 4s^2$, Zr: $4d^2 5s^2$, and S: $3s^2 3p^4$. These configurations were used to construct pseudopotentials and optimize electronic interactions in DFT calculations. The (S, Zr)-co-doped $CaTiO_3$ compounds are designated as $Ca_8Ti_7Zr_1O_{23}S_1$ and $Ca_8Ti_6Zr_2O_{22}S_2$, each with specific dopant concentrations.

Figure 1a, b shows the optimized supercells of undoped $CaTiO_3$ and co-doped (S, Zr) $CaTiO_3$, respectively. Analysis of structural changes after atomic relaxation revealed adjustments to interatomic distances and

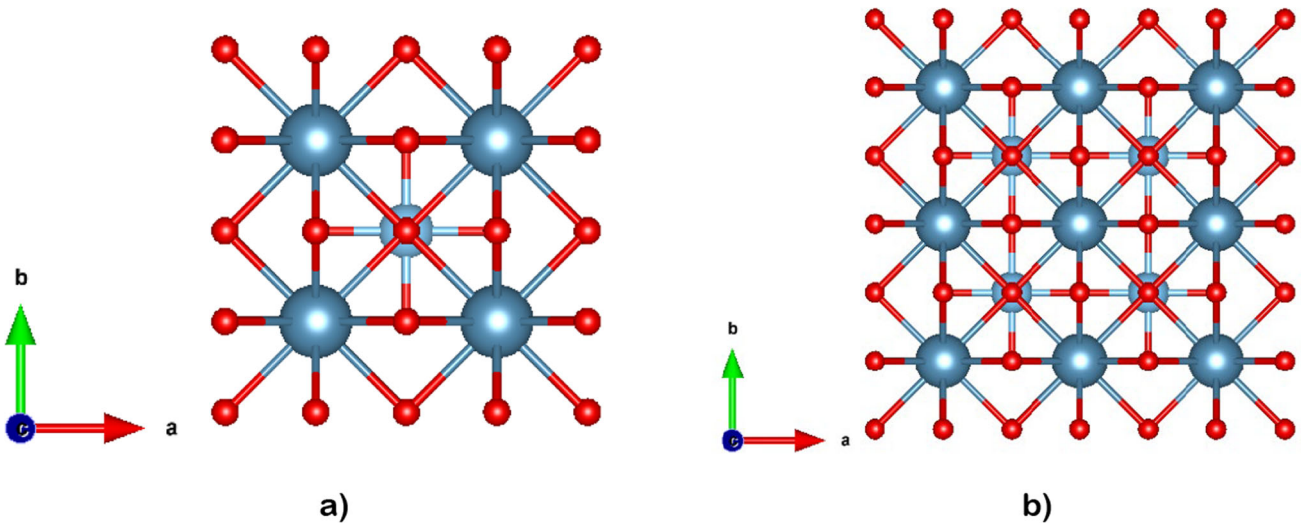

Fig. 1 Crystal structure of $CaTiO_3$: **a** unit cell and **b** $2 \times 2 \times 2$ supercell

Table 1 Optimized structural parameters of pure and S/Zr- co-doped $CaTiO_3$ systems

Compounds	$CaTiO_3$		$Ca_8Ti_7Zr_1O_{23}S_1$	$Ca_8Ti_6Zr_2O_{22}S_2$
Lattice constant (Å)	Our work	3.89	7.95	6.44
	Other study	3.856 [52] 3.899 [32]		
	Experimental	3.897 [54] 3.90 [55]		
Volume (Å^3)	58.86		503.2	267.2
B (GPa)	177.5		163.7	152.9
B'(GPa)	4.24		4.42	4.331
E_0 (Ry)	− 3520.7		− 34,303.4	− 20,221

bond angles, indicating a local reorganization of the crystal structure under the effect of co-doped. These results provide a better understanding of the impact of dopants on structural stability and open up prospects for perovskite engineering with a view to applications in photocatalysis and optoelectronics.

The improvement of lattice parameters and crystal volume plays a fundamental role in assessing the structural stability and physical properties of perovskite materials. These parameters are directly linked to key features such as electron density, atomic cohesion, and interatomic interactions, which influence the overall performance of the material in various technological applications. For cubic crystal structures, the unit cell volume V is given by $V = a^3$. Therefore, the volume of a $2 \times 2 \times 2$ supercell, $V_{\text{supercell}}$, is calculated as $V_{\text{supercell}} = (2a)^3 = 8a^3 = 8V_{\text{unit}}$, showing that the supercell volume is eight times that of the unit cell. Comparative analysis between experimental results and theoretical data obtained by DFT has enabled the lattice parameter of $CaTiO_3$ to be optimized, the values of which are listed in Table 1. These results show excellent agreement with experimental measurements, confirming the accuracy of the model used.

To determine the equilibrium lattice parameters, the pressure–volume relationship of the material was fitted using the Birch–Murnaghan equation of state. This approach makes it possible to optimize the crystal volume and accurately estimate the elastic properties, notably the modulus of compressibility and its pressure derivative. The Birch–Murnaghan equation of state is formulated as follows [50]:

$$E_{\text{tot}} = E_0 + \frac{9V_0B}{16}\left\{\left[\left(\frac{V_0}{V}\right)^{2/3} - 1\right]^2 B' + \left[\left(\frac{V_0}{V}\right)^{2/3} - 1\right]\left[6 - 4\left(\frac{V_0}{V}\right)^{2/3}\right]\right\}, \quad (1)$$

E indicates the material's total energy, E_0 is the energy of the ground state under zero pressure, V represents the volume, V_0 is the equilibrium volume, B is the bulk modulus, and B'is the pressure derivative of the bulk modulus [51]. Figures 2 and 3a, b show the optimization curve illustrating the total energy vs the volume of both undoped and co-doped $CaTiO_3$, demonstrating the stability of these materials. These

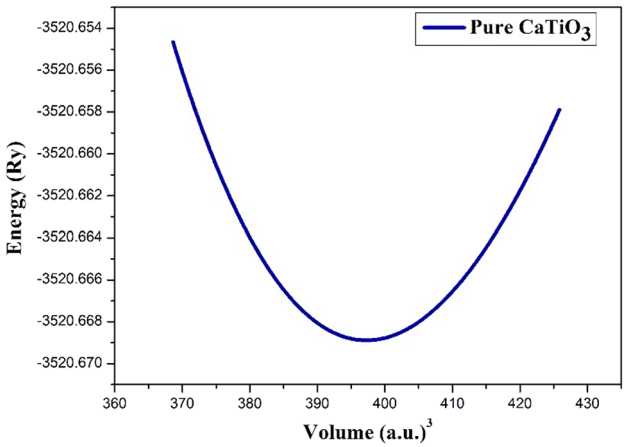

Fig. 2 Total energy variation of $CaTiO_3$ as a function of volume

findings align well with similar theoretical works [32, 34, 52, 53]. The co-doped $CaTiO_3$ shows larger lattice parameters than pure $CaTiO_3$ due to size differences between the dopant and host atoms. Zr^{4+} has a larger ionic radius than Ti^{4+}, while S^{2-} is slightly larger than O^{2-}. These differences in ionic radii lead to an expansion of the crystal lattice and an increase in unit cell volume. However, the reduction in lattice parameters of $Ca_8Ti_6Zr_2O_{22}S_2$ is due to lattice compression from atomic substitutions, indicating structural stabilization. This method provides a thorough way to analyze the optical properties of the materials studied, offering crucial insights into their potential effectiveness in photocatalytic applications.

The elastic constants C_{11}, C_{12}, and C_{44} for pure $CaTiO_3$ were calculated using the IRELAST software [56], a valid method for deriving elastic parameters from first-principles stress–strain data (see Table 2). These constants are critical for determining the mechanical stability of the materials. According to the Born stability criterion for cubic systems [57], the material is mechanically stable if the following requirements are met:$C_{11} > 0$, $C_{44} > 0$, $C_{11} - C_{12} > 0$, and $C_{11}+2C_{12} > 0$. Furthermore, the observation that pure $CaTiO_3$ fulfills the Born stability criterion for cubic crystals unequivocally demonstrates its mechanical stability, consistent with findings from previous studies [52, 58].

3.2 Formation energy

To analyze thermodynamic stability in detail, the material formation energy (Ef) was calculated using the following formula [59]:

$$E_{\mathrm{f}} = \frac{1}{N}\left[E_{\mathrm{Ca}_a\mathrm{Ti}_b\mathrm{Zr}_c\mathrm{O}_d\mathrm{S}_e} - (a \times \mu_{\mathrm{Ca}} + b \times \mu_{\mathrm{Ti}} + c \times \mu_{\mathrm{Zr}} + d \times \mu_{\mathrm{O}} + e \times \mu_{\mathrm{S}})\right], \quad (2)$$

where N is the total number of atoms and $E_{\mathrm{Ca}_a\mathrm{Ti}_b\mathrm{Zr}_c\mathrm{O}_d\mathrm{S}_e}$ represents the total energies of the co-doped materials. According to DFT calculations, the chemical potentials of Ca, Ti, Zr, O, and S are represented by the variables μ_{Ca},μ_{Ti},μ_{Zr},μ_{O}, and μ_{S}, respectively. The compound's thermodynamic stability compared to its constituent elements is indicated by a negative formation energy [60–63]. The calculated formation energies of both the pure and co-doped systems are negative, indicating their thermodynamic stability. Specifically, the pure structure has a formation energy of – 3.33 eV/atom, while the values for $Ca_8Ti_7Zr_1O_{23}S_1$ and $Ca_8Ti_6Zr_2O_{22}S_2$ are – 3.18 eV/atom and – 3.04 eV/atom, respectively (see Table 3). These results are in line with previous theoretical studies [59, 64–66], confirming the viability of co-doped structures for potential functional applications.

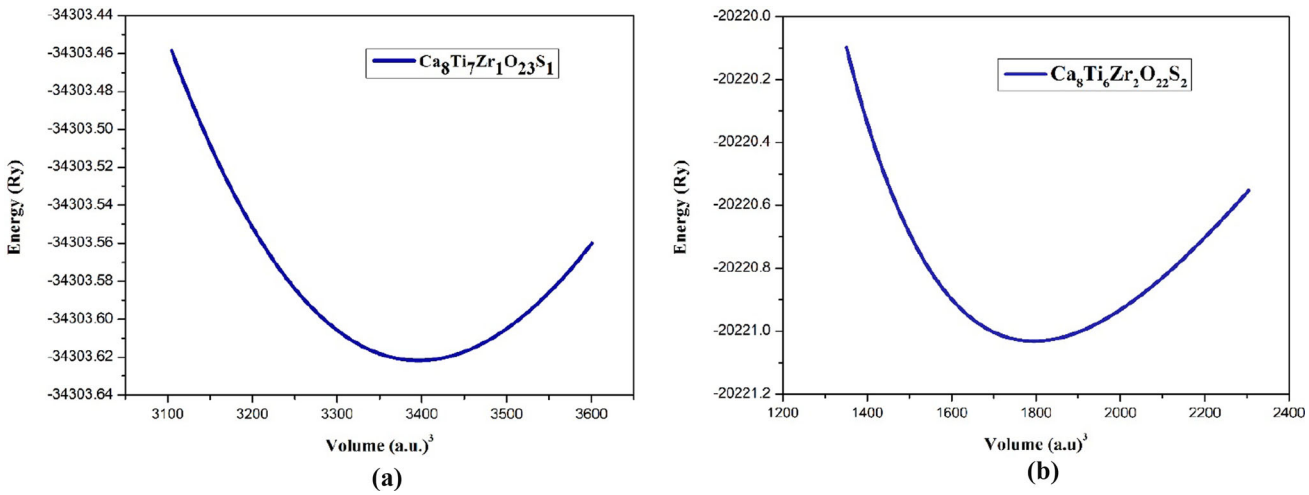

Fig. 3 Total energy variation of: **a)** $Ca_8Ti_7Zr_1O_{23}S_1$ and **b)** $Ca_8Ti_6Zr_2O_{22}S_2$ compounds as a function of volume

Table 2 Elastic constants of undoped $CaTiO_3$ (C_{11}, C_{12}, C_{44})

	C_{11}	C_{12}	C_{44}	$C_{11}-C_{12}$	$C_{11}+2C_{12}$
Our work	362.1	91.36	98.39	270.7	544.8
Other study	374.57 [52]	97.13 [52]	97.13 [52]	277.44 [52]	568.83 [52]

Table 3 Formation energy of the undoped and (S, Zr) co-doped $CaTiO_3$

Compounds	$CaTiO_3$	$Ca_8Ti_7Zr_1O_{23}S_1$	$Ca_8Ti_6Zr_2O_{22}S_2$
E_f (eV/atom)	− 3.33	− 3.18	− 3.04

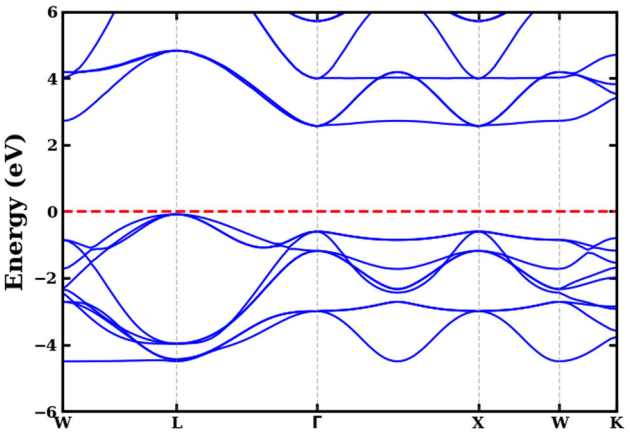

Fig. 4 Band structure of undoped $CaTiO_3$

3.3 Electronic properties

Analysis of the electronic band structures of undoped and co-doped (S, Zr) $CaTiO_3$ compounds highlights significant modifications induced by co-doping. Figures 3 and 4 show the band structures obtained, with the Fermi energy normalized to 0 eV on the vertical axis. These calculations were performed using the GGA and mBJ approach in the first Brillouin zone, following the W-L-Γ-X-W-K dispersion path, in line with previous theoretical studies [10, 41, 64, 67]. The bandgap energy (E_g) was determined for each compound, and it was observed that co-doping with S and Zr results in a significant reduction of the latter compared to undoped $CaTiO_3$ (see Table 4). This reduction in bandgap width can be explained by the introduction of the electronic states of the dopants into the crystal structure, thus modifying the density of electronic states and influencing the optoelectronic properties of the material. These results are in line with previous theoretical studies that have reported similar variations in bandgap energy for doped perovskites [10, 41, 64, 67].

Specifically, Fig. 4 reveals that undoped $CaTiO_3$ has an indirect band gap, with the valence band maximum (VBM) located at the L point and the conduction band minimum (CBM) at the Γ point, which is in agreement with previous theoretical work [53, 68]. In co-doped systems (S, Zr), on the other hand, the band structure shows a significant change, where both the VBM and CBM lie at the Γ point, indicating a transition to a direct bandgap (see Fig. 5). This development suggests that co-doping alters the nature of orbital interactions and enhances direct electronic transitions. Such behavior is particularly advantageous for optoelectronic and photocatalytic applications, as a direct bandgap material promotes more efficient light absorption and charge carrier separation.

Thus, the transformation of the band gap, combined with the reduction of its width, indicates that (S, Zr) co-doping is an effective strategy for tuning the electronic properties of $CaTiO_3$, paving the way for its use in next-generation photovoltaic devices, optical sensors, and photocatalysts. These results confirm that the chemical and structural modification induced by co-doping profoundly influences the material's electronic and optical characteristics, making it more effective for advanced technological applications.

Total density of states (TDOS) and projected density of states (PDOS) computation of the (S, Zr) co-doped $CaTiO_3$ materials have identified individual atomic orbitals' contribution towards the electronic band structure. Such a contribution, along with the electronic transition from the conduction band to the valence band in the present work, indicated the co-doping effect's implication on the material's electronic property. Figures 6 and 7 show, respectively, PDOS and TDOS of undoped and (S, Zr) co-doped $CaTiO_3$ materials within an energy scale of − 6 eV to 6 eV with a dotted line indicating the Fermi level. For undoped $CaTiO_3$, it can be seen that the calculation gives the oxygen p-orbital contribution (O-p) majority occupation of the valence band in TDOS, while titanium d orbitals (Ti-d) fill the majority part of the conduction band. A prominent hybridization of O-p and Ti-d states has been seen here, implying high electronic interaction between the two atoms. This co-doping-induced hybridization is perovskite-like and plays a central role

Table 4 Calculated band gap energy of the undoped and (S, Zr)-co-doped $CaTiO_3$

Compounds	$CaTiO_3$	$Ca_8Ti_7Zr_1O_{23}S_1$	$Ca_8Ti_6Zr_2O_{22}S_2$
E_g (eV)	2.77	2.22	1.85

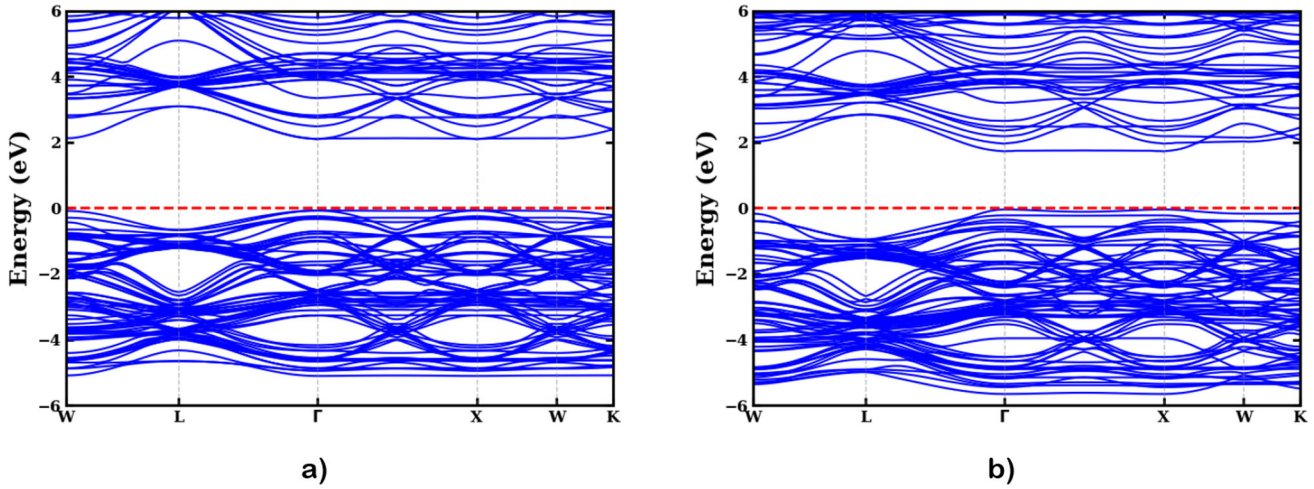

Fig. 5 Band structure of **a** $Ca_8Ti_7Zr_1O_{23}S_1$ and **b** $Ca_8Ti_6Zr_2O_{22}S_2$

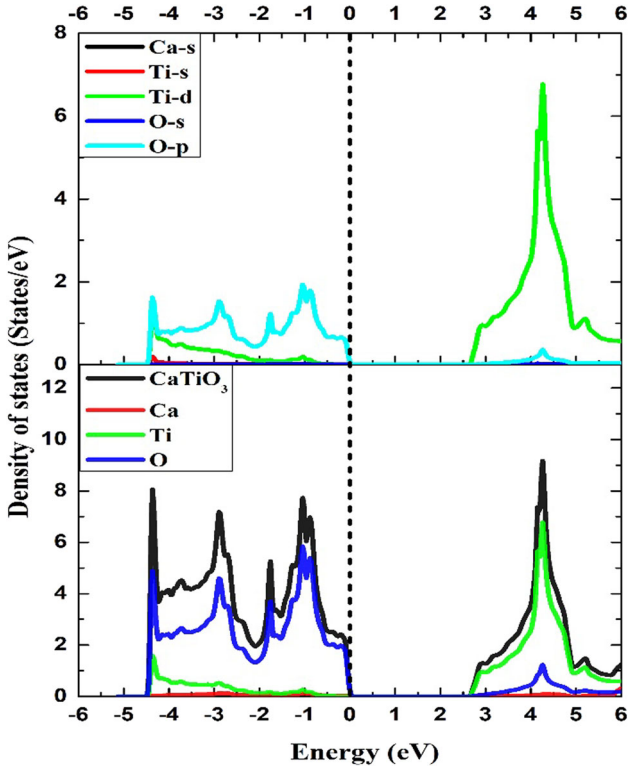

Fig. 6 TDOS and PDOS of undoped $CaTiO_3$

in modulating the material's electronic as well as optical properties.

The introduction of co-doping (S, Zr) induces dramatic changes in the electronic structure. Especially in the case of co-doped $CaTiO_3$, the valence band bottom, from −5.5 eV to −4.5 eV, is defined by sulfur p-orbital contributions (S-p) indicative of the doping impact on electronic state distribution. The valence band edge (– 4.5 eV to 0 eV) remains dominated by O-p orbitals but with some contribution from Ca, Ti, Zr, O, and S s-orbitals, although small in magnitude. Intensive hybridization between the S-p and O-p states is revealed in the valence band, which can affect charge carrier mobility and enhance the optical absorption of the compound. For the conduction band, it is also dominated predominantly by titanium *d* orbitals (Ti-d), which again confirms that Ti remains to be at the center of the electronic transitions in the system. The Fermi level position significantly shifts, approaching the top of the valence band, meaning that the material possesses p-type semiconductor behavior. It is brought about by the charge compensation effect caused by the introduction of Zr and S substituting for Ti and O, thus altering the distribution profile of the electrons. Furthermore, the S-p states are positioned near the top of the valence band, while the Zr-d states are situated close to the conduction band minimum. These dopant-induced states effectively reduce the band gap by elevating the valence band and lowering the conduction band. Consequently, the band gap decreases from 2.77eV (pure $CaTiO_3$) to 2.22 and 1.85 eV (S/Zr co-doped $CaTiO_3$) (see Table 4). The narrowing of the band gap corresponds to the increased visible light absorption observed in the co-doped system, indicating improved optical behavior. This electronic modification, as evidenced by the TDOS and PDOS, indicates a promising potential for optoelectronic and photocatalytic applications. Specifically, the TDOS spectrum distinctly indicates a decreased energy gap between the VB and CB edges, while the PDOS demonstrates that this phenomenon is due to the emergence of S-p and Zr-d states near the band edges, thereby validating the impact of co-doping on the electronic structure.

3.4 Optical properties

The optical properties of materials are determined by their dielectric function, which comprises a real part, $\varepsilon_1(\omega)$, and an imaginary part, $\varepsilon_2(\omega)$. These parameters play a fundamental role in the material's interaction with light, and are used to describe various optical

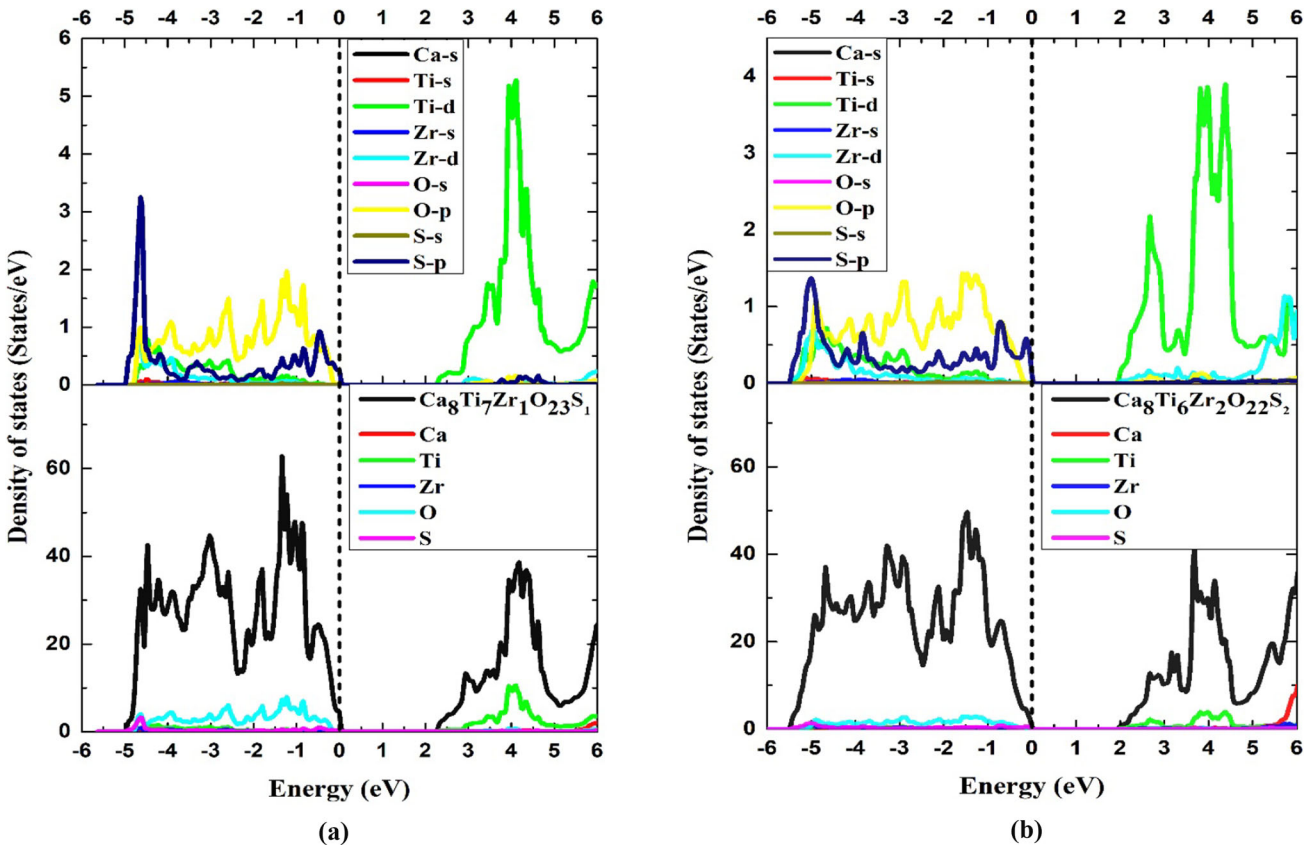

Fig. 7 TDOS and PDOS for **a** $Ca_8Ti_7Zr_1O_{23}S_1$ and **b** $Ca_8Ti_6Zr_2O_{22}S_2$

phenomena such as absorption, reflectivity, refractive index, and optical conductivity [69, 70]. The complex dielectric function is expressed as follows:

$$\varepsilon(\omega) = \varepsilon_1(\omega) + i\varepsilon_2(\omega) \tag{3}$$

The imaginary part, $\varepsilon_2(\omega)$, is directly influenced by the band structure of the material. It is calculated from the momentum matrix elements linking the occupied and empty electronic states, according to the following equation [71]:

$$\varepsilon_2(\omega) = \left(\frac{2e^2\pi}{\varepsilon_0\Omega}\right) \sum_{k,v,c} \Psi_k^c |u.r| \Psi_k^{v2} \delta(E_k^c - E_k^v - \hbar\omega) \tag{4}$$

In this equation, the frequency-dependent complex dielectric function $\varepsilon(\omega)$, influenced by light frequency (ω), electron charge (e), CB and VB wave functions Ψ_k^c and Ψ_k^v, and incident electric field polarization (u), determines optical properties (absorption, reflectivity, conductivity, refractive index) and is governed by Kramers–Kronig relations ($\varepsilon_1(\omega)$ from $\varepsilon_2(\omega)$).

Figure 8a illustrates the evolution of $\varepsilon_1(\omega)$, which represents the material's ability to store electrical energy. A value of $\varepsilon_1(\omega) > 1$ indicates that the material can store more energy than a material with $\varepsilon_1(\omega) = 1$, which is particularly advantageous for photovoltaic and photocatalytic applications, as it promotes better interaction with incident light, thus optimizing absorption and charge separation [72]. After co-doping with S and Zr, the maximum value of $\varepsilon_1(\omega)$ is reached at 3.46 eV for $Ca_8Ti_6Zr_2O_{22}S_2$ and 3.60 eV for $Ca_8Ti_7Zr_1O_{23}S_1$ in the zz direction. In addition, $Ca_8Ti_6Zr_2O_{22}S_2$ shows a significant increase in $\varepsilon_1(\omega)$ around 1 eV, which enhances its absorption in the visible range compared to $Ca_8Ti_7Zr_1O_{23}S_1$. However, after this maximum value, $\varepsilon_1(\omega)$ rapidly decreases below zero for all curves. Co-doped $CaTiO_3$ compounds (S, Zr) exhibit negative $\varepsilon_1(\omega)$ values between 7 and 14 eV, suggesting electromagnetic wave damping and the possibility of longitudinally polarized waves [73, 74].

Figure 8b shows $\varepsilon_2(\omega)$ plots. For undoped $CaTiO_3$, the curves of ε_2 (ω) in the xx and zz directions are virtually identical, indicating isotropic behavior. An energy threshold of around 2.77 eV is observed, corresponding to the material's band gap (Fig. 6), resulting from intrinsic electronic transitions between the O-2p (VBM) and Ti-3d (CBM) states. After co-doping with S and Zr, a reduction in threshold energy is observed in the xx and zz directions, which is in agreement with the decrease in bandgap revealed in Fig. 7a, b. In addition, co-doped materials show absorption peaks in the ultraviolet (UV) and visible range, reflecting improved interband electronic transitions and better optical response

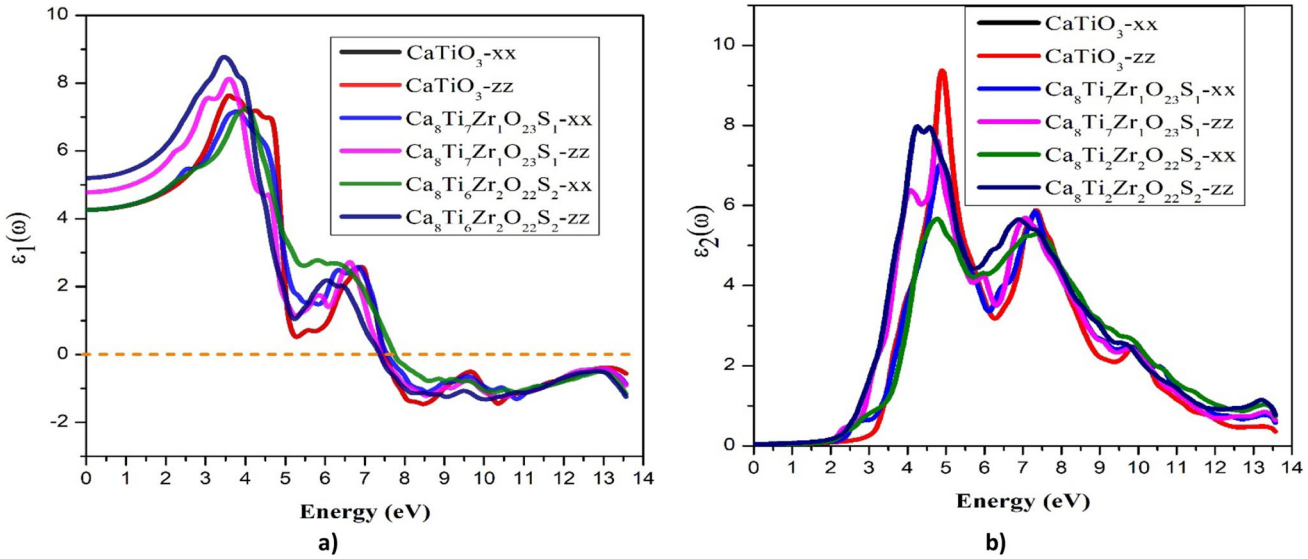

Fig. 8 Dielectric function—**a** real and **b** imaginary components for undoped and co-doped $CaTiO_3$

in the visible range. The most intense UV absorption peak is recorded in the zz direction, highlighting the optical anisotropy of the material after co-doping.

Table 4 summarizes the bandgap energy (E_g) calculated for undoped $CaTiO_3$ and co-doped systems. A progressive decrease in E_g with co-doping:

This bandgap reduction indicates that co-doping promotes a shift in optical absorption towards lower energies, which improves the material's response to visible light and makes it a promising candidate for applications in photovoltaics and photocatalysis.

The absorption coefficient $\alpha(\omega)$ is a key measure of a material's ability to absorb light and directly influences its efficiency in optical and photocatalytic applications. The $\alpha(\omega)$ is determined using the following relationship:

$$\alpha(\omega) = (2)^{1/2}\omega\left[\sqrt{\varepsilon_1(\omega)^2 + \varepsilon_2(\omega)^2} - \varepsilon_1(\omega)\right]^{1/2}. \quad (5)$$

Figure 9a shows the $\alpha(\omega)$ plots. Undoped $CaTiO_3$ absorbs ultraviolet radiation along the xx and zz directions. Co-doping with S and Zr reduces the bandgap (see Table 3), shifting the $\alpha(\omega)$ into the visible range, thus enabling co-doped $CaTiO_3$ to absorb more photons. Furthermore, $Ca_8Ti_6Zr_2O_{22}S_2$ shows enhanced absorption in the visible range along the zz direction compared to $Ca_8Ti_7Zr_1O_{23}S_1$ along both xx and zz directions and $Ca_8Ti_6Zr_2O_{22}S_2$ along the xx directions. The enhanced absorption indicates that co-doping with S and Zr markedly boosts the light absorption capacity of $CaTiO_3$, showcasing its potential for photocatalytic applications. In addition, these findings align with prior theoretical and experimental studies and are comparable to those of perovskites [10, 45, 64, 67, 75, 76].

The optical conductivity coefficient, $\sigma(\omega)$, is a crucial parameter for assessing a material's ability to conduct electricity under the influence of an oscillating electric field, such as that generated by light. It determines the material's interaction with photons and is particularly important in photocatalytic applications where a strong optical response is required for the conversion of light energy into chemical energy. The $\sigma(\omega)$ is generated from the $\varepsilon_2(\omega)$, using the relationship [77, 78]:

$$\sigma(\omega) = \frac{\omega}{4\pi}\varepsilon_2(\omega). \quad (6)$$

For undoped $CaTiO_3$, $\sigma(\omega)$ analysis shows that optical conductivity is significant only in the ultraviolet (UV) range, as illustrated in Fig. 9b. This is consistent with the material's wide bandgap, which limits its interaction with visible light. Indeed, the energy of photons in the UV range is sufficient to excite electrons from the valence band (VB) to the conduction band (CB), thus enabling notable optical conductivity in this range. However, this limited response in the UV range restricts the effectiveness of $CaTiO_3$ in photocatalytic applications where broader absorption of the light spectrum is required to maximize light energy conversion efficiency.

In contrast, for $CaTiO_3$ co-doped with S and Zr, the figure shows that $\sigma(\omega)$ now extends into the visible range. This change is attributed to the reduction in bandgap width due to co-doping with S) and Zr, enabling the material to absorb photons in a wider range of wavelengths. This extension of the optical conductivity range is a major advantage for photocatalytic applications, as it enables the material to interact not only with UV light, but also with a significant portion of visible light, thus increasing its efficiency in processes such as the degradation of pollutants or the production of energy from water. The extension of $\sigma(\omega)$ to the visible range offers several advantages. It increases the photocatalytic efficiency of the material, facilitating the use of wider sunlight. In addition, it improves

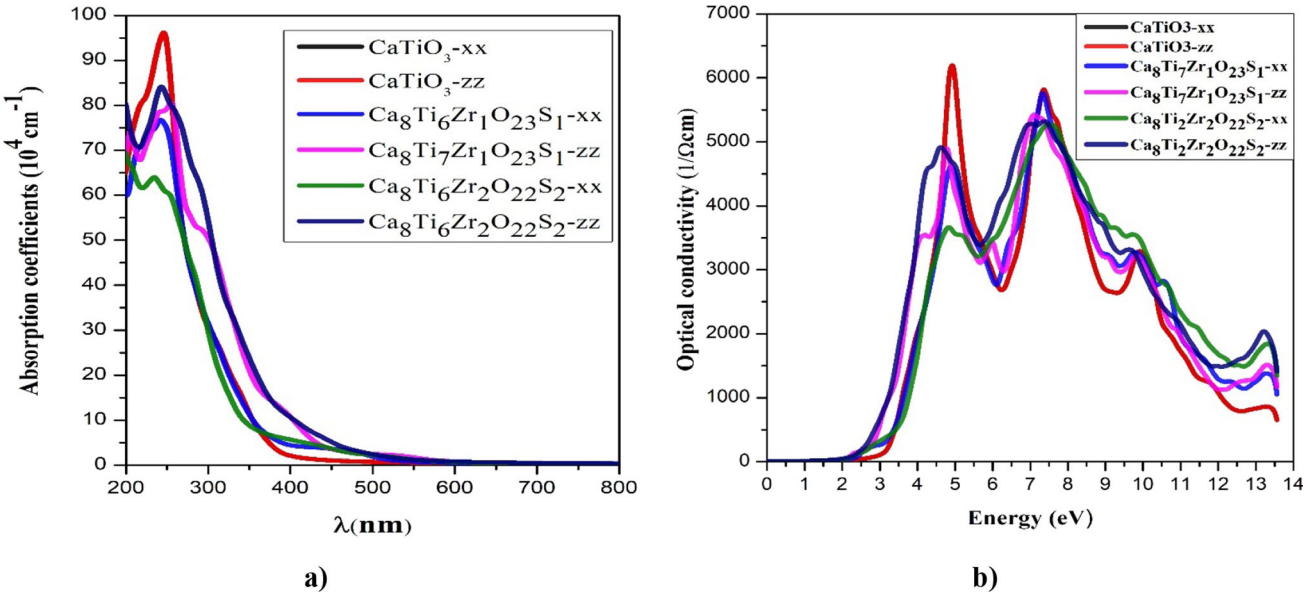

Fig. 9 **a** Absorption coefficient, and **b** optical conductivity for the undoped and co-doped $CaTiO_3$

the separation of charges generated under light irradiation, which is essential for optimizing photocatalytic reactions. In summary, co-doping with S and Zr offers a significant improvement in the light absorption capacity and photocatalytic performance of $CaTiO_3$, making it more suitable for practical applications in solar energy conversion. These findings are in line with previous theoretical research [20–22, 79]. Moreover, recent studies in nonlinear physics have highlighted how dopant-induced perturbations and lattice distortions can give rise to complex, non-additive behaviors in functional materials, which are relevant to the present work on co-doped perovskites [80–85].

3.5 Thermodynamic properties

To examine the thermodynamic behavior of the S- and Zr-co-doped $CaTiO_3$ perovskite, we used the quasi-harmonic Debye approximation and first-principles DFT calculations, as implemented in the GIBBS suite approach [86–88]. The Grüneisen parameter (γ), Debye temperature (Θ_D), entropy (S), specific heat capacities C_p and C_v, and thermal expansion coefficient (α) were thoroughly examined throughout an extensive range of temperatures (0–1000 K) and pressures (0–20 Gpa) [59, 89, 90].

The Grüneisen parameter, γ, shown in Fig. 10, measures the anharmonicity of lattice vibrations and their sensitivity to external stimuli. At ambient pressure, γ in pure $CaTiO_3$ increases slightly with temperature, from about 2.05 at 0 K to around 2.15 at 1000 K and 0 GPa. γ decreases with increasing pressure. A similar behavior is observed in the doped materials, where γ decreases with increasing pressure, while the temperature-dependent trend of γ remains consistent.

Figure 11 shows the changes in the Debye temperature for S- and Zr-co-doped $CaTiO_3$ perovskite in relation to temperature and pressure. In pure $CaTiO_3$, Θ_D remains constant at low temperatures but decreases somewhat with rising temperatures, signifying gradual lattice softening. At moderate pressure (5 GPa), a slight increase in Θ_D indicates improved vibrational stiffness; however, at elevated pressures (10–20 GPa), Θ_D experiences a more pronounced increase due to lattice compression. In doped $Ca_8Ti_7Zr_1O_{23}S_1$, Θ_D is somewhat reduced compared to pure $CaTiO_3$, beginning at 700 K and declining to 675 K at 0 Gpa. In $Ca_8Ti_6Zr_2O_{22}S_2$, Θ_D is decreased significantly, varying from 675 to 625 K at 0 Gpa. However, as pressure intensifies, Θ_D progressively increases, signifying augmented lattice stiffness, but it diminishes with rising temperature.

Figure 12 illustrates the variation of entropy (S) with temperature. At 0 GPa and 300 K, the entropy (S) values are 65 J/mol.K for $CaTiO_3$, 650 J/mol.K for $Ca_8Ti_7Zr_1O_{23}S_1$, and 380 J/mol.K for $Ca_8Ti_6Zr_2O_{22}S_2$. As temperature rises, entropy increases for all materials because of phonon excitation, although the rate of increase differs. $Ca_8Ti_7Zr_1O_{23}S_1$ has the greatest entropy increase, indicating augmented lattice disorder resulting from Zr and S doping, whereas $CaTiO_3$ displays the minimal increase owing to its more ordered structure. $Ca_8Ti_6Zr_2O_{22}S_2$, despite having higher initial entropy than pure $CaTiO_3$, experiences a more moderate increase, as stronger bonding interactions partially suppress disorder.

The heat capacities (C_p and C_v) of $CaTiO_3$, $Ca_8Ti_7Zr_1O_{23}S_1$, and $Ca_8Ti_6Zr_2O_{22}S_2$ at pressures ranging from 0 to 20 GPa show clear patterns with doping and pressure in Figs. 13 and 14. In $CaTiO_3$, both C_p and C_v rise with temperature, with minor pressure effects, and approach the Dulong–Petit limit (~ 125 J/mol.K). Zr and S doping in $Ca_8Ti_7Zr_1O_{23}S_1$

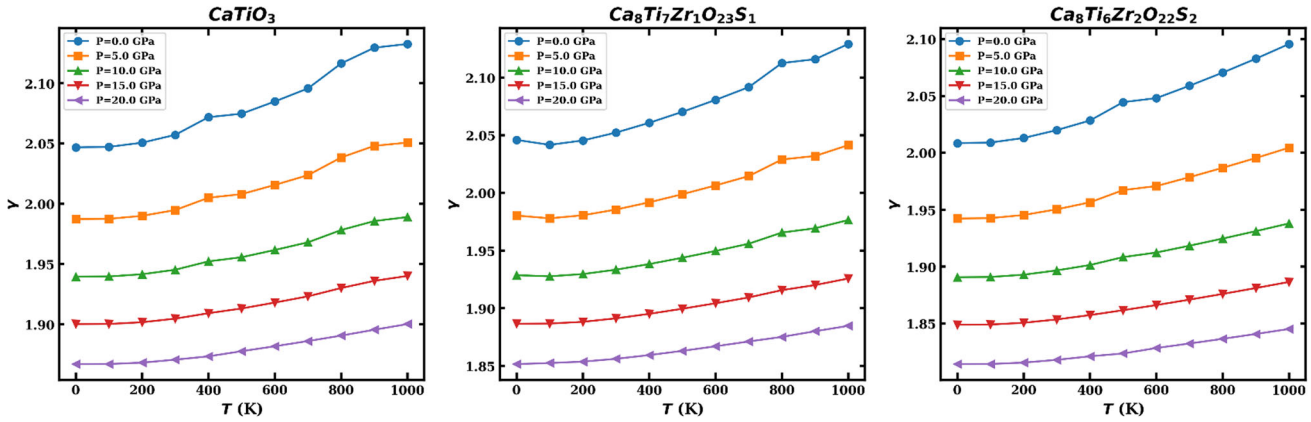

Fig. 10 Grüneisen parameter (γ) of undoped $CaTiO_3$ and co-doped (S, Zr) materials varies with temperature and pressure

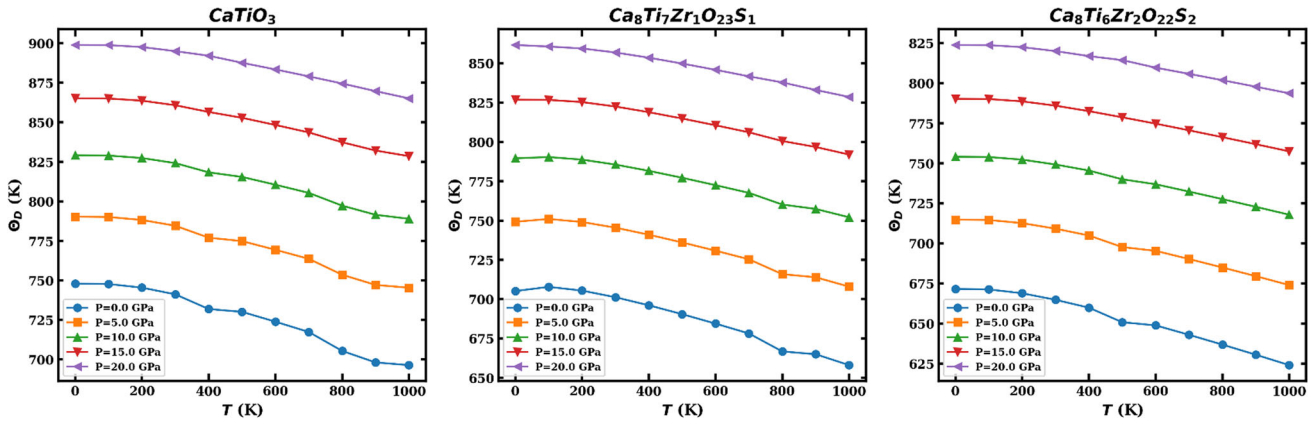

Fig. 11 Debye temperature (Θ_D) of undoped $CaTiO_3$ and co-doped (S, Zr) materials varies with temperature and pressure

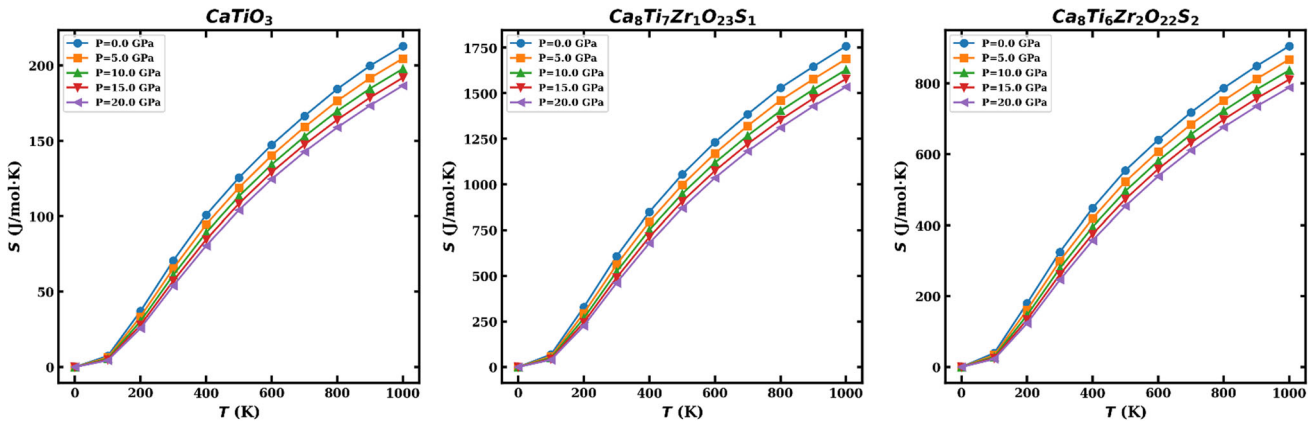

Fig. 12 Entropy (S) of undoped $CaTiO_3$ and co-doped (S, Zr) materials varies with temperature and pressure

greatly increases heat capacity, reaching approximately 1000 J/mol.K at 1000 K, most likely as a result of increased phonon contributions. However, higher doping in $Ca_8Ti_6Zr_2O_{22}S_2$ reduces C_p (500 J/mol.K at 1000 K), suggesting lattice stiffening that limit phonon excitations. Pressure slightly lowers C_p and C_v at low temperatures, but has little influence at high temperatures. In general, moderate Zr/S co-doping increases heat capacity, whereas severe doping reduces thermal storage efficiency by limiting phonon dynamics.

Ultimately, we analyzed the thermal expansion coefficient (α) as illustrated in Fig. 15 to comprehend lattice expansion resulting from anharmonic vibrations. In $CaTiO_3$, the coefficient α increases with temperature, reaching a maximum between 800 and 1000 K, but diminishes under pressure due to lattice compression, which attenuates thermal vibrations.

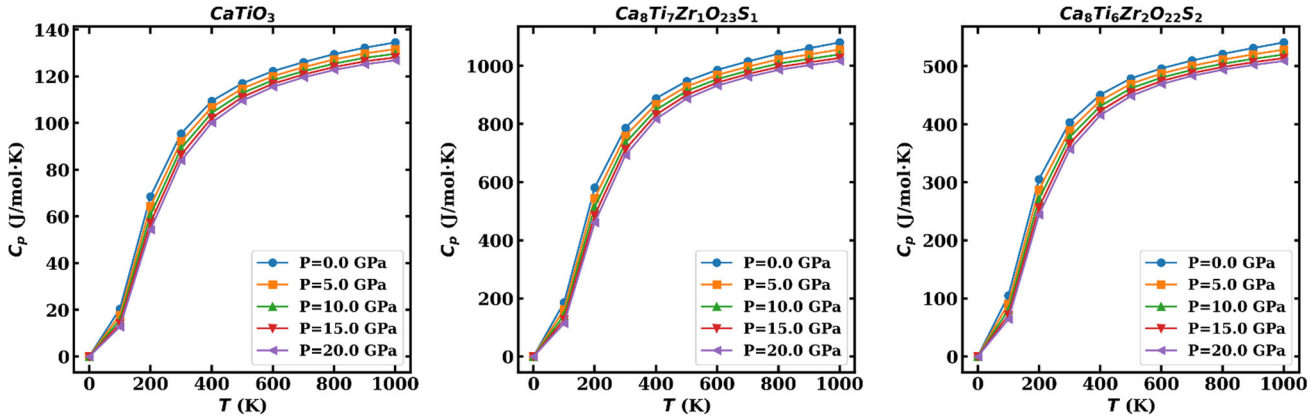

Fig. 13 Heat capacity (C_{p}) of undoped $CaTiO_3$ and co-doped (S, Zr) materials varies with temperature and pressure

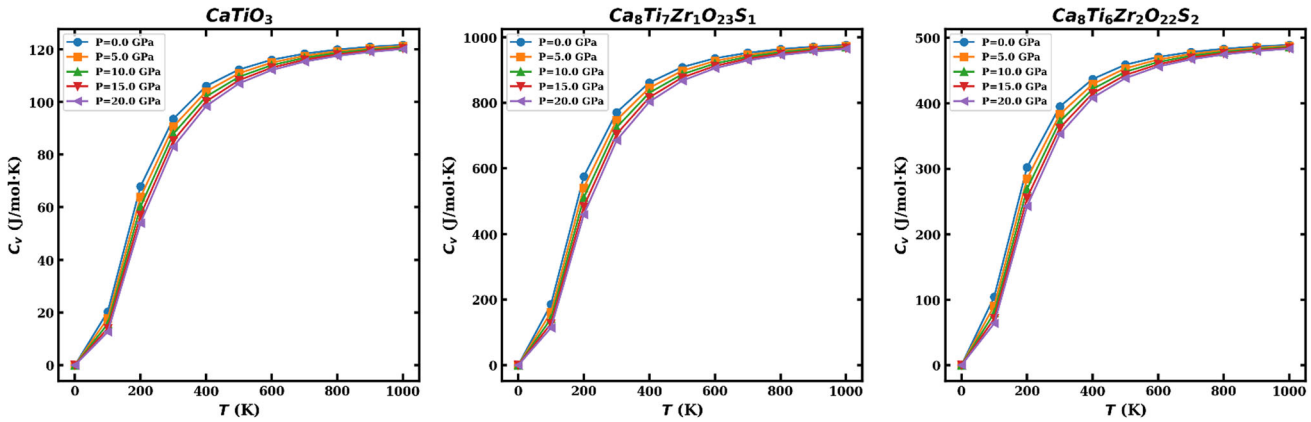

Fig. 14 Heat capacity (C_{v}) of undoped $CaTiO_3$ and co-doped (S, Zr) materials varies with temperature and pressure

In $Ca_8Ti_7Zr_1O_{23}S_1$, doping with Zr and S somewhat improves α at low temperatures, however the enhancement is less pronounced at elevated temperatures. Under pressure, α drops further, indicating a stiffer lattice. In highly doped $Ca_8Ti_6Zr_2O_{22}S_2$, the α is first reduced due to enhanced bonding and increases more gradually with temperature. At 10–20 GPa, this system exhibits the lowest α, rendering it exceptionally resistant to thermal expansion-suitable for applications necessitating dimensional stability. Our computed thermodynamic parameters, including the trends of γ, Θ_{D}, entropy, heat capacities, and expansion coefficient α, align well with the results of Zeeshan Abbas et al. for pure $CaTiO_3$ [91]. This consistency strengthens the reliability of our quasi-harmonic Debye methodology and underscores the precision of our first-principles computations in representing the thermodynamic behavior of the doped system.

3.6 Photocatalytic properties

Photocatalytic (PC) water splitting is a promising and efficient method for producing renewable hydrogen by harnessing solar energy and suitable semiconductor materials [92]. For a material to be an effective photocatalyst, it must absorb sunlight optimally, particularly in the visible spectrum, and exhibit appropriate energy levels to promote redox reactions. The bandgap energy of the material is a key factor in this process. For a water splitting reaction to be thermodynamically favorable, the bandgap energy must be between 1.23 and 3 eV [93]. Although optical absorption analysis provides important insights into a material's suitability for optoelectronic applications, it is inadequate by itself for evaluating photocatalytic performance. A comprehensive assessment of the band edge potentials is crucial, since they dictate the material's capacity to enable the oxidation and reduction half-reactions required for effective water splitting. This condition guarantees efficient absorption of solar energy while maintaining sufficient energy to activate water dissociation reactions. In addition to this constraint on the band gap, the positions of the band edges are crucial: the VBM must be more positive than the oxidation potential of water, which is 1.23 eV relative to the normal hydrogen electrode (NHE). In addition, the CBM must be more negative than the H^+/H_2 proton reduction potential, which is 0 eV relative to the NHE [94]. These conditions

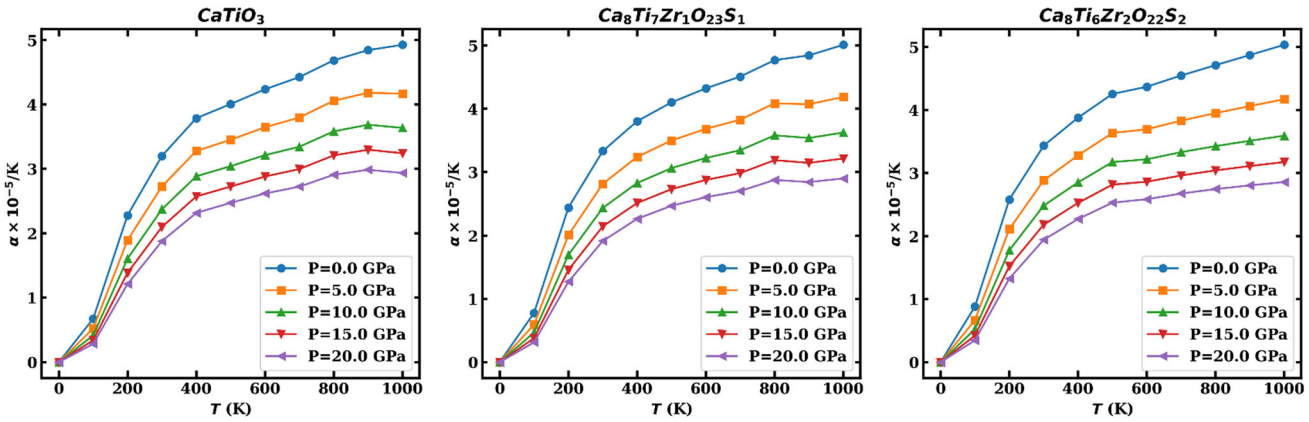

Fig. 15 The thermal expansion coefficient (α) of undoped $CaTiO_3$ and co-doped (S, Zr) materials varies with temperature and pressure

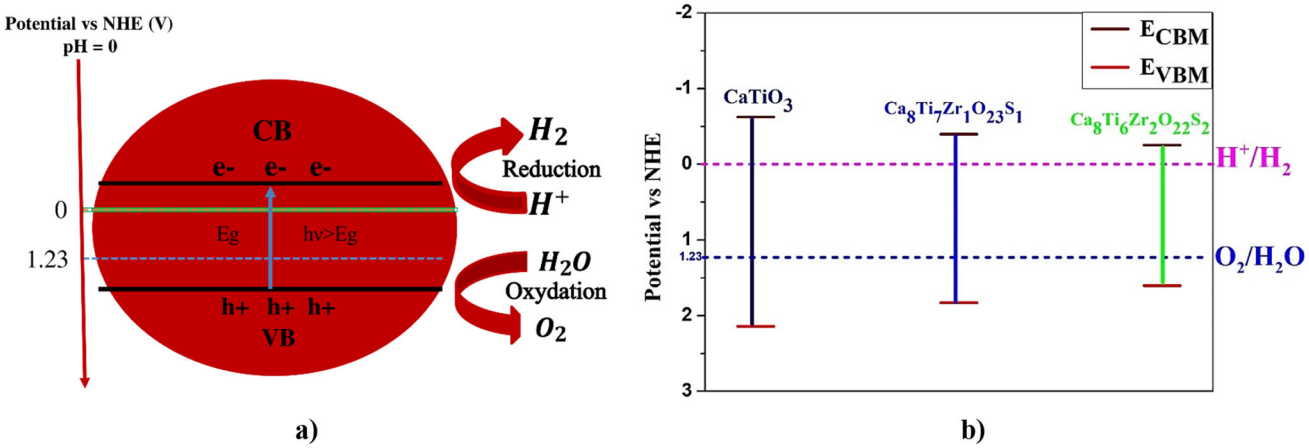

Fig. 16 **a** Process diagram for photocatalytic water splitting, and **b** band alignment of the CBM and VBM potentials for undoped and (S, Zr) co-doped $CaTiO_3$

ensure efficient charge separation and optimal reactivity for water dissociation, as illustrated in Fig. 16a.

Consider the semiconductor with the chemical composition $Ca_aTi_bZr_cO_dS_e$, where a, b, c, d, and e represent the stoichiometric coefficients of Ca, Ti, Zr, O and S, respectively.

- The absolute electronegativity (χ_e) of a semiconductor be calculated as the geometric mean of the electronegativities of its constituent atoms, as described by [95, 96]:

$$\chi_{CaTiO_3} = \left\{\chi_{Ca} \times \chi_{Ti} \times (\chi_O)^3\right\}^{\frac{1}{5}} \tag{7}$$

$$\chi_{Ca_aTi_bZr_cO_dS_e} = \left\{(\chi_{Ca})^a \times (\chi_{Ti})^b \times (\chi_{Zr})^c \times (\chi_O)^d \times (\chi_S)^e\right\}^{\frac{1}{(a+b+c+d+e)}}, \tag{8}$$

where χ_{Ca}, χ_{Ti}, χ_{Zr}, χ_O, and χ_S represent the absolute electronegativities of Ca, Ti, Zr, O, and S elements, respectively, as determined by Bartolotti [97].

- By determining the band gap (E_g) of the material and utilizing the vacuum reference energy $E_0 = 4.5$ eV, the valence band maximum (E_{VB}) and conduction band minimum (E_{CB}) are calculated as follows [96, 98]:

$$E_{CB} = (\chi_e - E_0) - 0.5E_g \tag{9}$$

$$E_{VB} = (\chi_e - E_0) + 0.5E_g \tag{10}$$

- The resulting band edge positions, expressed in terms of vacuum level, can be converted into redox potentials in terms of normal hydrogen electrode (NHE) using the Nernst equation. To achieve efficient photocatalytic water splitting, the following conditions must be met:

$$E_{CB} < 0eV \text{ Vs NHE}, E_{VB} > +1.23 \text{ eV vs NHE}.$$

Figure 16b illustrates the energy levels of the E_{CB} and E_{VB} for undoped and (S, Zr)-co-doped $CaTiO_3$,

Table 5 Calculated electronegativity (χ_e), band gap energy, E_{VB}, and E_{CB} for (S, Zr) co-doped $CaTiO_3$

Compounds	E_g (eV)	χ_e (eV)	E_{CB} (eV)	E_{VB} (eV)
$CaTiO_3$	2.77	5.26	− 0.62	2.14
$Ca_8Ti_7Zr_1O_{23}S_1$	2.22	5.22	− 0.39	1.83
$Ca_8Ti_6Zr_2O_{22}S_2$	1.85	5.17	− 0.25	1.60

with Table 5 summarizing these values, indicating significant increases in E_{VB} potential when going from undoped $CaTiO_3$ to co-doped compounds, particularly in the order undoped $CaTiO_3$ < $Ca_8Ti_7Zr_1O_{23}S_1$ < $Ca_8Ti_6Zr_2O_{22}S_2$, while the E_{CB} potential decreases noticeably in the same order. This increase in E_{VB} shows an enhanced ability to generate holes in the E_{VB} to oxidize water and produce O_2, which is essential for photocatalytic applications. Similarly, the alignment of E_{CB} values with the potentials required for the reduction of H^+ protons to H_2 shows that the co-dopings investigated improve the performance of $CaTiO_3$ for the photodissociation of water. So, the co-doping with (S, Zr) optimizes photocatalytic properties by enhancing catalytic activity under visible light. Furthermore, the CBM is shifted downward for the $Ca_8Ti_7Zr_1O_{23}S_1$ compound and further moved in the same direction due to the $Ca_8Ti_6Zr_2O_{22}S_2$ compound. This trend indicates an enhancement in the photoreduction capability. Moreover, the CBM of $Ca_8Ti_7Zr_1O_{23}S_1$ (0.229 eV) and $Ca_8Ti_6Zr_2O_{22}S_2$ (0.371 eV) exceeds the standard hydrogen reduction potential (H^+/H_2) compared to undoped $CaTiO_3$. This advantageous energy state allows CB electrons to reduce H^+ ions, producing H_2 gas through the following reaction:

$$2H^+ + 2e^- \rightarrow H_2. \tag{11}$$

Furthermore, the VBM is shifted upward for both the $Ca_8Ti_7Zr_1O_{23}S_1$ and $Ca_8Ti_6Zr_2O_{22}S_2$ compounds, indicating an enhancement in photooxidation capacity. In addition, the VBM of both compounds is below the water oxidation level of the (O_2/H_2O) couple, allowing holes in the VB to oxidize water (H_2O) to produce oxygen gas (O_2), as shown in the following reaction:

$$H_2O + 2h^+ \rightarrow 2H^+ + \frac{1}{2}O_2. \tag{12}$$

Consequently, due to their enhanced photocatalytic properties and comparison with Ref [10, 38, 95, 99, 100], water can be decomposed into H_2 and O_2 by $CaTiO_3$ compounds that are co-doped with (S, Zr). Finally, co-doping $CaTiO_3$ with Se and Zr favorably modifies its electronic band structure, aligning band edges for overall water splitting. Specifically, $Ca_8Ti_6Zr_2O_{22}S_2$ exhibits a narrowed band gap of 1.85 eV, enhancing visible light absorption and broadening the photoresponse range. This combination of optimized band alignment and improved optical properties significantly enhances photocatalytic performance. Compared to previous studies, S and Zr co-doping effectively tunes the band gap and boosts photocatalytic activity, demonstrating the potential of targeted co-doping for designing efficient perovskite-based photocatalysts for sustainable hydrogen production.

4 Conclusion

In summary, DFT calculations using the Wien2k code provided a comprehensive understanding of the structural, optoelectronic, thermodynamic, and photocatalytic properties of both undoped and S/Zr co-doped $CaTiO_3$ materials. The calculated formation energies of pure and S/Zr co-doped $CaTiO_3$ indicate thermodynamic stability. Co-doping with S and Zr reduces the band gap energy from 2.77 eV for pure $CaTiO_3$ to 2.22 eV for $Ca_8Ti_7Zr_1O_{23}S_1$ and 1.85 eV for $Ca_8Ti_6Zr_2O_{22}S_2$, respectively. This reduction enhances the material's optical and electrical properties. The findings also show that co-doping improves both the absorption coefficient and optical conductivity in the visible light spectrum. Furthermore, the calculated band edge positions meet the requirements for water splitting with energy levels appropriate for both reduction and oxidation, as its E_{VB} and E_{CB} are above and below the potentials of H_2O/O_2 and H^+/H_2, respectively. Among the studied compounds, $Ca_8Ti_6Zr_2O_{22}S_2$ shows the best performance, with a lower band gap and stronger light absorption, making it a promising photocatalyst. Moreover, thermodynamic analysis reveals a substantial alteration in the Grüneisen parameter, Debye temperature, entropy, and heat capacities as a result of co-doping, demonstrating the modification of lattice anharmonicity and vibrational properties with fluctuations in temperature and pressure. These variations, which do not follow a linear trend with dopant concentration, suggest nonlinear interactions between the dopants and the host lattice, contributing to the emergent properties of the co-doped systems. These findings indicate that S/Zr co-doped $CaTiO_3$ could be useful in renewable energy technologies, especially solar-driven photocatalytic hydrogen production. Furthermore, its improved optoelectronic properties suggest that it has promising applications in photovoltaic and optoelectronic devices.

Acknowledgements The authors are warmly grateful to the support of ***"The Moroccan Association of Sciences and Techniques for Sustainable Development (MASTSD), Beni Mellal, Morocco,"*** and to its president, Professor ***Charaf Laghlimi***, for the valuable proposals. Also, our acknowledgments are for Professor ***Wedad***

El-Osta from ***"The Libyan Center for Solar Energy Research and Studies, Tajoura—Tripoli-Libya*** http://csers.ly/en/***"***

Author contributions

A. Bouzaid: writing the original draft, and validation. Y. Ziat: supervising. H. Belkhanchi: analyzing and validation. H. Fatihi: validation.

Data availability The data that support the findings of this study are available on request.

Code availability The calculations were performed using the WIEN2k code (version 21.1), which is available under license from the developers via https://www.wien2k.at.

Declarations

Conflict of interest The authors have no conflicts of interest to declare.

References

1. A. Koufi, Y. Ziat, H. Belkhanchi, M. Miri, N. Lakouari, F.Z. Baghli, A computational study of the structural and thermal conduct of $MgCrH_3$ and $MgFeH_3$ perovskite-type hydrides: FP-LAPW and BoltzTraP insight. E3S Web Conf. **582**, 02003 (2024). https://doi.org/10.1051/e3sconf/202458202003
2. A. Raihan, J. Rahman, T. Tanchangtya, M. Ridwan, S. Islam, An overview of the recent development and prospects of renewable energy in Italy. Renew. Sustain. Energy **2**(2), 0008 (2024). https://doi.org/10.55092/rse20240008
3. D. Gayen, R. Chatterjee, S. Roy, A review on environmental impacts of renewable energy for sustainable development. Int. J. Environ. Sci. Technol. **21**(5), 5285–5310 (2024). https://doi.org/10.1016/j.rser.2021.110868
4. U.M. Adanma, E.O. Ogunbiyi, Assessing the economic and environmental impacts of renewable energy adoption across different global regions. Eng. Sci. Technol. J. **5**(5), 1767–1793 (2024). https://doi.org/10.51594/estj/v5i5.1154
5. H. Wang, L. Zhang, Z. Chen, J. Hu, S. Li, Z. Wang, J. Liu, X. Wang, Semiconductor heterojunction photocatalysts: design, construction, and photocatalytic performances. Chem. Soc. Rev. **43**(15), 5234–5244 (2014). https://doi.org/10.1039/C4CS00126E
6. V. Kumaravel, S. Mathew, J. Bartlett, S.C. Pillai, Photocatalytic hydrogen production using metal doped TiO_2: a review of recent advances. Appl. Catal. B Environ. **244**, 1021–1064 (2019). https://doi.org/10.1016/j.apcatb.2018.11.080
7. A. Fujishima, K. Honda, Electrochemical photolysis of water at a semiconductor electrode. Nature **238**(5358), 37–38 (1972). https://doi.org/10.1038/238037a0
8. W. Jiang, W. Luo, J. Wang, M. Zhang, Y. Zhu, Enhancement of catalytic activity and oxidative ability for graphitic carbon nitride. J. Photochem. Photobiol. C, Photochem. Rev. **28**, 87–115 (2016). https://doi.org/10.1016/j.jphotochemrev.2016.06.001
9. J. Low, S. Cao, J. Yu, S. Wageh, Two-dimensional layered composite photocatalysts. Chem. Commun. **50**(74), 10768–10777 (2014). https://doi.org/10.1039/C4CC02553A
10. H. Bentour, M. El Yadari, A. El Kenz, A. Benyoussef, DFT study of electronic and optical properties of (S–Mn) co-doped $SrTiO_3$ for enhanced photocatalytic hydrogen production. Solid State Commun. **312**, 113893 (2020). https://doi.org/10.1016/j.ssc.2020.113893
11. A. Bouzaid, Y. Ziat, H. Belkhanchi, Prediction the effect of (S, Se, Te) doped MgTiO3 on optoelectronic, catalytic, and pH conduct as promised candidate photovoltaic device: Ab initio framework. Int. J. Hydrogen Energy **100**, 20–32 (2025). https://doi.org/10.1016/j.ijhydene.2024.12.284
12. S.F. Hosseini, M.A. Wahid, Hydrogen production from renewable and sustainable energy resources: promising green energy carrier for clean development. Renew. Sustain. Energy Rev. **57**, 850–866 (2016). https://doi.org/10.1016/j.rser.2015.12.112
13. C. Laghlimi, A. Moutcine, Y. Ziat, H. Belkhanchi, A. Koufi, S. Bouyassan, Hydrogen, chronology and electrochemical production. Solar Energy Sustain. Dev. (2024). https://doi.org/10.51646/jsesd.v14iSI_MSMS2E.405
14. I. Alani, M.M. Dzagli, D.M. Kongnine, S. Narra, Z. Asiedu, Biomethane and green hydrogen production potential from municipal solid waste in Cape Coast, Ghana. J. Solar Energy Sustain. Dev. **13**(2), 102–119 (2024). https://doi.org/10.51646/jsesd.v13i2.204
15. F. Yang, Y. Pan, I.P. Jain, Single atom enhanced the catalytic activity of borophene catalysts for hydrogen evolution reaction. Int. J. Hydrogen Energy **140**, 223–232 (2025). https://doi.org/10.1016/j.ijhydene.2025.05.339
16. L. Azzouz, M. Halit, M. Rérat, R. Khenata, A.K. Singh, M.M. Obeid, H.R. Jappor, X. Wang, Structural, electronic and optical properties of $ABTe_2$ (A= Li, Na, K, Rb, Cs and B= Sc, Y, La): insights from first-principles computations. J. Solid State Chem. **279**, 120954 (2019). https://doi.org/10.1016/j.jssc.2019.120954
17. H.R. Jappor, A.O.M. Almayyali, H.A. Mezher, S. Al-Qaisi, S. Bin-Omran, R. Khenata, Prediction of 2D XC_2N_4 (X= Ti, Mo, and W) monolayers with high mobility as an encouraging candidate for photovoltaic devices. Surf. Interface Anal. **54**, 105261 (2024). https://doi.org/10.1016/j.surfin.2024.105261
18. A.K. Kushwaha, S.P. Mishra, M.K. Vishwakarma, S. Chauhan, H.R. Jappor, R. Khenata, S.B. Omran, Theoretical study of thermal conductivity, mechanical, vibrational and thermodynamical properties of $Ln_2Zr_2O_7$ (Ln= La, Nd, Sm, and Eu), pyrochlore. Inorg. Chem. Commun. **127**, 108495 (2021). https://doi.org/10.1016/j.inoche.2021.108495
19. A. Koufi, Y. Ziat, H. Belkhanchi, Study of the Gravimetric, Electronic and Thermoelectric Properties of

XAlH3 (X = Be, Na, K) as hydrogen storage perovskite using DFT and the BoltzTrap Software Package. Solar Energy Sustain. Dev., Dev. **14**(SI_MSMS2E), 53–66 (2024). https://doi.org/10.51646/jsesd.v14iSI_MSMS2E.403
20. A. Boutramine, S. Al-Qaisi, N. Algethami, S. Tastift, A.H. Alfaifi, H.S. Alzahrani, H. Chaib, H.R. Jappor, H. Rached, First-principles investigation of K2InSbZ6 (Z= I, Br, Cl, F) eco-friendly halide double perovskites: structural, thermodynamic, optoelectronic and thermoelectric properties for efficient energy harvesting applications. Phys. B Condens. Matter (2025). https://doi.org/10.1016/j.physb.2025.417280
21. S. Al-Qaisi, N. Iram, N. Sfina, A. Boutramine, H.R. Jappor, A.H. Alfaifi, H.S. Alzahrani, H. Rached, M.A. Ali, G. Murtaza, Comprehensive DFT study of K2TlZI6 (Z= Al, In) double perovskites: structural stability and potential for optoelectronic and thermoelectric energy harvesting. Physica B **710**, 417239 (2025). https://doi.org/10.1016/j.physb.2025.417239
22. A. Es-Smairi, S. Al-Qaisi, N. Sfina, A. Boutramine, H.R. Jappor, H.S. Alzahrani, A.H. Alfaifi, H. Rached, A.S. Verma, M. Archi, M.F. Rahman, DFT insights into the structural, stability, elastic, and optoelectronic characteristics, of Na_2LiZF_6 (Z= Ir and Rh) double perovskites for sustainable energy. J. Comput. Chem. **46**(8), e70097 (2025). https://doi.org/10.1002/jcc.70097
23. V. Tiwari, B. Pal, S. Kaur, Photocatalysis of Ag-loaded $MgTiO_3$ for degradation of fuchsin dye and dyes present in textile wastewater under sunlight. Sol. Energy **296**, 113587 (2025). https://doi.org/10.1016/j.solener.2025.113587
24. D. D. Nematov, A.S. Burhonzoda, F. Shokir. Analysis of the structural characteristics and optoelectronic properties of $CaTiO_3$ as a non-toxic raw material for solar cells: a DFT study. arXiv preprint arXiv:2210.14835 (2022). https://doi.org/10.48550/arXiv.2210.14835.
25. M. Hasan, S. Nasrin, M.N. Islam, A.K.M. Hossain, First-principles insights into the electronic, optical, mechanical, and thermodynamic properties of lead-free cubic ABO3 [A= Ba, Ca, Sr; B= Ce, Ti, Zr] perovskites. AIP Adv. (2022). https://doi.org/10.1063/5.0104191
26. A. Bouzaid, Y. Ziat, H. Belkhanchi, Photovoltaic potential of doped $MgTiO_3$ (F, Br, I): prediction of optoelectronic and catalytic within *ab initio* approach. J. Phys. Chem. Solids **201**, 112648 (2025). https://doi.org/10.1016/j.jpcs.2025.112648
27. F. Opoku, K.K. Govender, C.G.C.E. van Sittert, P.P. Govender, Recent progress in the development of semiconductor-based photocatalyst materials for applications in photocatalytic water splitting and degradation of pollutants. Adv. Sustain. Syst. **1**(7), 1700006 (2017). https://doi.org/10.1002/adsu.201700006
28. X. Li, H. Zhao, J. Liang, Y. Luo, G. Chen, X. Shi, S. Lu, S. Gao, J. Hu, X. Sun, A-site perovskite oxides: an emerging functional material for electrocatalysis and photocatalysis. J. Mater. Chem. A **9**(11), 6650–6670 (2021). https://doi.org/10.1039/D0TA09756J
29. Y. Li, B. Deng, J. Wang, J. Li, J. Fan, J. Han, Effects of Mo doping on the structure, adsorption performance, and photocatalytic activity of $LaFeO_3$ nanoparticles: experimental and DFT studies. Sep. Purif. Technol. **347**, 127304 (2024). https://doi.org/10.1016/j.seppur.2024.127304
30. H. Mizoguchi, K. Ueda, M. Orita, S.C. Moon, K. Kajihara, M. Hirano, H. Hosono, Decomposition of water by a $CaTiO_3$ photocatalyst under UV light irradiation. Mater. Res. Bull. **37**(15), 2401–2406 (2002). https://doi.org/10.1016/S0025-5408(02)00974-1
31. Y. Wang, Q. Zhou, Q. Zhang, Y. Ren, K. Cui, C. Cheng, K. Wu, Effects of La-N co-doping of $BaTiO_3$ on its electron-optical properties for photocatalysis: a DFT study. Molecules **29**(10), 2250 (2024). https://doi.org/10.3390/molecules29102250
32. Q. Zhang, Y. Wang, Y. Jia, W. Yan, Q. Li, J. Zhou, K. Wu, Engineering the electronic structure towards visible lights photocatalysis of $CaTiO_3$ perovskites by cation (La/Ce)-anion (N/S) co-doping: a first-principles study. Molecules **28**(20), 7134 (2023). https://doi.org/10.3390/molecules28207134
33. W. Yang, W. Cui, L. Yang, G. Zhang, X. Li, Y. Shen, F. Dong, Y. Sun, The structural differences of perovskite $ATiO_3$ (A= Ca, Sr) dictate the photocatalytic VOCs mineralization efficiency. Chem. Eng. J. **425**, 130613 (2021). https://doi.org/10.1016/j.cej.2021.130613
34. L. Attou, A. Al-Shami, J. Boujemaâ, O. Mounkachi, H. Ez-Zahraouy, Predicting the structural, optoelectronic, dynamical stability and transport properties of Boron-doped CaTiO3: DFT based study. Phys. Scr. **97**(11), 115808 (2022). https://doi.org/10.1088/1402-4896/ac95d8
35. H. Zhang, G. Chen, Y. Li, Y. Teng, Electronic structure and photocatalytic properties of copper-doped $CaTiO_3$. Int. J. Hydrogen Energy **35**(7), 2713–2716 (2010). https://doi.org/10.1016/j.ijhydene.2009.04.050
36. A. Zhu, J. Wang, Y. Du, D. Zhao, Q. Gao, Effects of Zn impurities on the electronic properties of Pr doped $CaTiO_3$. Phys. B **407**(5), 849–854 (2012). https://doi.org/10.1016/j.physb.2011.12.096
37. W. Zulfiqar, S.M. Alay-e-Abbas, Improved thermodynamic stability and visible light absorption in Zr+X codoped (X= S, Se and Te) $BaTiO_3$ photocatalysts: a first-principles study. Mater. Today Commun. **32**, 103867 (2022). https://doi.org/10.1016/j.mtcomm.2022.103867
38. W. Zulfiqar, F. Javed, G. Abbas, J.A. Larsson, S.M. Alay-e-Abbas, Stabilizing the dopability of chalcogens in $BaZrO_3$ through Ti_{Zr} co-doping and its impact on the opto-electronic and photocatalytic properties: a meta-GGA level DFT study. Int. J. Hydrogen Energy **58**, 409–415 (2024). https://doi.org/10.1016/j.ijhydene.2024.01.202
39. J.U. Rehman, M.A. Rehman, M.B. Tahir, A. Hussain, T. Iqbal, M. Sagir, M. Usman, I. Kebaili, H. Alrobei, M. Alzaid, Electronic and optical properties of nitrogen and sulfur doped strontium titanate as efficient photocatalyst for water splitting: a DFT study. Int. J. Hydrogen Energy **47**(3), 1605–1612 (2022). https://doi.org/10.1016/j.ijhydene.2021.10.133
40. G.A. Alves, H.A. Centurion, J.R. Sambrano, M.M. Ferrer, R.V. Gonçalves, Band gap narrowing of Bi-doped $NaTaO_3$ for photocatalytic hydrogen evolution under simulated sunlight: a pseudocubic phase induced

by doping. ACS Appl. Energy Mater. **4**(1), 671–679 (2020). https://doi.org/10.1021/acsaem.0c02547
41. B. Mouhib, S. Dahbi, A. Douayar, N. Tahiri, O. El Bounagui, H. Ez-Zahraouy, Theoretical investigations of electronic structure and optical properties of S, Se or Te doped perovskite $ATiO_3$ (A= Ca, Ba, and Sr) materials for eco-friendly solar cells. Micro Nanostruct. **163**, 107124 (2022). https://doi.org/10.1016/j.spmi.2021.107124
42. S. Zafar, I. Zeba, M. Zaman, M. Shakil, S.S.A. Gillani, First principles computation of novel hydrogen-doped $CsSrO_3$ with excellent optoelectronic properties as a potential photocatalyst for water splitting. Phys. Scr. **99**(7), 075942 (2024). https://doi.org/10.1088/1402-4896/ad5257
43. A. Ou-Khouya, I. Ait Brahim, H. Ez-Zahraouy, A. Houba, H. Mes-Adi, M. Tahiri, First-principles calculations to investigate impact of doping by chalcogen elements on the electronic, structural, and optical properties of $SrTiO_3$ compounds. Chem. Phys. **581**, 112253 (2024). https://doi.org/10.1016/j.chemphys.2024.112253
44. C. Yan, Q. Zeng, J. Zhu, Q. Cao, Influence of Zr–S co-doping on the electronic structure and optical properties of anatase TiO_2: first-principles GGA+ U method. Appl. Phys. A **125**, 1–9 (2019). https://doi.org/10.1007/s00339-019-2416-0
45. N. Orangi, H. Farrokhpour, Mono-doped (X= S^{2-}, Se^{2-}, and Te^{2-}) and co-doped (Zr^{4+}-X) TiO_2 monolayer nanosheet for water splitting: DFT modeling. J. Iran. Chem. Soc. **21**(10), 2643–2657 (2024). https://doi.org/10.1007/s13738-024-03096-6
46. W. Kohn, A.D. Becke, R.G. Parr, Density functional theory of electronic structure. J. Phys. Chem. **100**(31), 12974–12980 (1996). https://doi.org/10.1021/jp960669l
47. P. Blaha, K. Schwarz, G. K. H. Madsen, D. Kvasnicka, and J. Luitz, *WIEN2k: An Augmented Plane Wave + Local Orbitals Program for Calculating Crystal Properties*, Vienna University of Technology, Austria (2002), ISBN 3-9501031-1-2.
48. J.P. Perdew, K. Burke, M. Ernzerhof, Generalized gradient approximation made simple (vol 77, pg 3865, 1996). Phys. Rev. Lett. **78**(7), 1396–1396 (1997). https://doi.org/10.1103/PhysRevLett.77.3865
49. D. Koller, F. Tran, P. Blaha, Improving the modified Becke-Johnson exchange potential. Phys. Rev. B—Condens. Matter Mater. Phys. **85**(15), 155109 (2012). https://doi.org/10.1103/PhysRevB.85.155109
50. F.D. Murnaghan, The compressibility of media under extreme pressures. Proc. Natl. Acad. Sci. **30**(9), 244–247 (1944). https://doi.org/10.1073/pnas.30.9.24
51. P.H. Mott, J.R. Dorgan, C.M. Roland, The bulk modulus and Poisson's ratio of "incompressible" materials. J. Sound Vib. **312**(4–5), 572–575 (2008)
52. A.A. Adewale, A. Chik, T. Adam, O.K. Yusuff, S.A. Ayinde, Y.K. Sanusi, First principles calculations of structural, electronic, mechanical and thermoelectric properties of cubic $ATiO_3$ (A= Be, Mg, Ca, Sr and Ba) perovskite oxide. Comput. Condenss. Matter **28**, e00562 (2021). https://doi.org/10.1016/j.cocom.2021.e00562
53. M. Rizwan, H.N. Ullah, S.S.A. Gillani, S. Ahmad, T. Mahmood, Photocatalytic and optical properties of (Mg: La) $CaTiO_3$: Insights from first principles studies. J. Phys. Chem. Solids **169**, 110830 (2022). https://doi.org/10.1016/j.jpcs.2022.110830
54. R. Ali, M. Yashima, Space group and crystal structure of the perovskite $CaTiO_3$ from 296 to 1720 K. J. Solid State Chem. **178**(9), 2867–2872 (2005). https://doi.org/10.1016/j.jssc.2005.06.027
55. B.J. Kennedy, C.J. Howard, B.C. Chakoumakos, Phase transitions in perovskite at elevated temperatures-a powder neutron diffraction study. J. Phys. Condens. Matter **11**(6), 1479 (1999). https://doi.org/10.1088/0953-8984/11/6/012
56. M. Jamal, M. Bilal, I. Ahmad, S. Jalali-Asadabadi, Irelast package. J. Alloys Compd. **735**, 569–579 (2018). https://doi.org/10.1016/j.jallcom.2017.10.139
57. M. Born, K. Huang, Dynamical theory of crystal lattices. Oxford University Press. (1996). https://doi.org/10.1093/oso/9780192670083.001.0001
58. A.P. Sakhya, Electronic structure and elastic properties of $ATiO_3$ (A= Ba, Sr, Ca) perovskites: a first principles study. Indian J. Pure Appl. Phys. (IJPAP) **53**(2), 102–109 (2015)
59. A. Chelh, B. Akenoun, S. Dahbi, H. Ez-Zahraouy, First-principles calculations to investigate photovoltaic, photocatalytic, and spintronic properties of Fe-doped and alloyed $MgSiO_3$ perovskite. J. Phys. Chem. Solids (2025). https://doi.org/10.1016/j.jpcs.2025.112773
60. Q. Mahmood, M. Yaseen, B.U. Haq, A. Laref, A. Nazir, The study of mechanical and thermoelectric behavior of $MgXO_3$ (X= Si, Ge, Sn) for energy applications by DFT. Chem. Phys. **524**, 106–112 (2019). https://doi.org/10.1016/j.chemphys.2019.05.009
61. A. Bouzaid, Y. Ziat, H. Belkhanchi, H. Hamdani, A. Koufi, M. Miri, Z. Zarhri, Ab initio study of the structural, electronic, and optical properties of MgTiO3 perovskite materials doped with N and P. E3S Web Conf. **582**, 02006 (2024). https://doi.org/10.1051/e3sconf/202458202006
62. M.A. Moiz, A. Mumtaz, M. Salman, S.W. Husain, A.H. Baluch, M. Ramzan, Band gap engineering of ZnO via transition metal doping: an ab initio study. Chem. Phys. Lett. **781**, 138979 (2021). https://doi.org/10.1016/j.cplett.2021.138979
63. Z. Zarhri, A.D. Cano, O. Oubram, Y. Ziat, A. Bassam, Optical measurements and Burstein Moss effect in optical properties of Nb-doped $BaSnO_3$ perovskite. Micro Nanostruct. **166**, 207223 (2021). https://doi.org/10.1016/j.micrna.2022.207223
64. F. Mezzat, H. Zaari, A. El Kenz, A. Benyoussef, Enhanced visible light photocatalytic activity of $KTaO_3$ (Se, V): DFT investigation. Comput. Condens. Matter **30**, e00648 (2022). https://doi.org/10.1016/j.cocom.2022.e00648
65. S. Dahbi, N. Tahiri, O. El Bounagui, H. Ez-Zahraouy, Effects of oxygen group elements on thermodynamic stability, electronic structures and optical properties of the pure and pressed BaTiO3 perovskite. Comput. Condens. Matter **32**, e00728 (2022). https://doi.org/10.1016/j.cocom.2022.e00728

66. Z. Ech-charqy, A. El Badraoui, A. Elkhou, M. Ziati, H. Ez-Zahraouy, Effect of sulfur doping on the electronic structures, optical and photocatalytic properties of $KTaO_3$ perovskites: DFT calculations. Chem. Phys. (2025). https://doi.org/10.1016/j.chemphys.2025.112759
67. C. Zhang, Y. Jia, Y. Jing, Y. Yao, J. Ma, J. Sun, Effect of non-metal elements (B, C, N, F, P, S) mono-doping as anions on electronic structure of $SrTiO_3$. Comput. Mater. Sci. **79**, 69–74 (2013). https://doi.org/10.1016/j.commatsci.2013.06.009
68. S. Tariq, A. Ahmed, S. Saad, S. Tariq, Structural, electronic and elastic properties of the cubic $CaTiO_3$ under pressure: a DFT study. AIP Adv. (2015). https://doi.org/10.1063/1.4926437
69. Y. Ziat, H. Belkhanchi, Z. Zarhri, DFT analysis of structural, electrical, and optical properties of S, Si, and F-doped GeO_2 rutile: implications for UV-transparent conductors and photodetection. Sol. Energy Sust. Dev. **14**(1), 74–89 (2025). https://doi.org/10.51646/jsesd.v14i1.232
70. Y. Ziat, H. Belkhanchi, Z. Zarhri, & C. Laghlimi. Theoretical Study of the Optical, Structural and Electronic Properties of Germanium Dioxide (GeO_2) Doped with Ti and Nb by the DFT Method with mBJ Correction. In NanoRevolution (pp. 195–211)., CRC Press (2025). https://doi.org/10.1201/9781003499732-11/.
71. M. Hasan, A.A. Hossain, Structural, electronic and optical properties of strontium and nickel co-doped $BaTiO_3$: a DFT based study. Comput. Condens. Matter **28**, e00578 (2021). https://doi.org/10.1016/j.cocom.2021.e00578
72. H. Fatihi, M. Agouri, H. Ouhenou, H. Benaali, A. Zaghrane, A. Abbassi, M. El Idrissi, S. Taj, B. Manaut, Enhancing solar cell efficiency: a comparative study of lead-free double halide perovskites, Rb2CuAsBr 6 and Rb2Tl AsBr6 using DFT and SLME methods. J. Inorg. Organomet. Polym. Mater. (2024). https://doi.org/10.1007/s10904-024-03330-x
73. A. Zaghrane, H. Ouhenou, E. Darkaoui, A. Abbassi, S. Taj, B. Manaut, A. Razouk, Comprehensive investigation of Rb_2LuCl5 and Rb2PrCl5 rare earth-based scintillation materials using density functional theory. Mater. Res. Bull. **181**, 113071 (2025). https://doi.org/10.1016/j.materresbull.2024.113071
74. E. Zahedi, M. Hojamberdiev, M.F. Bekheet, Electronic, optical and photocatalytic properties of three-layer perovskite Dion-Jacobson phase $CsBa_2$ M_3O_{10} (M= Ta, Nb): a DFT study. RSC Adv. **5**(108), 88725–88735 (2015). https://doi.org/10.1039/C5RA13763B
75. R. Konta, T. Ishii, H. Kato, A. Kudo, Photocatalytic activities of noble metal ion doped $SrTiO_3$ under visible light irradiation. J. Phys. Chem. B **108**(26), 8992–8995 (2004). https://doi.org/10.1021/jp049556p
76. J. Wang, H. Li, H. Li, S. Yin, T. Sato, Preparation and photocatalytic activity of visible light-active sulfur and nitrogen co-doped $SrTiO_3$. Solid State Sci. **11**(1), 182–188 (2009). https://doi.org/10.1016/j.solidstatesciences.2008.04.010
77. C.M.I. Okoye, Theoretical study of the electronic structure, chemical bonding and optical properties of $KNbO_3$ in the paraelectric cubic phase. J. Phys. Condens. Matter **15**(35), 5945 (2003). https://doi.org/10.1088/0953-8984/15/35/304
78. A. Delin, O. Eriksson, R. Ahuja, B. Johansson, M.S.S. Brooks, T. Gasche, S. Auluck, J.M. Wills, Optical properties of the group-IVB refractory metal compounds. Phys. Rev. B **54**(3), 1673 (1996). https://doi.org/10.1103/PhysRevB.54.1673
79. J. Yang, X. Li, Y. Yang, R. Dou, Strain engineering the optoelectronic and HER behavior of MoS_2/ZnO heterojunction: a DFT investigation. J. Phys. Chem. Lett. **16**(11), 2731–2741 (2025). https://doi.org/10.1021/acs.jpclett.4c03605
80. X.Y. Gao, Hetero-Bäcklund transformation, bilinear forms and multi-solitons for a (2+ 1)-dimensional generalized modified dispersive water-wave system for the shallow water. Chin. J. Phys. **92**, 1233–1239 (2024). https://doi.org/10.1016/j.cjph.2024.10.004
81. X.Y. Gao, Open-ocean shallow-water dynamics via a (2+1)-dimensional generalized variable-coefficient Hirota-Satsuma-Ito system: oceanic auto-Bäcklund transformation and oceanic solitons. Chin. Ocean Eng. **39**(3), 541–547 (2025). https://doi.org/10.1007/s13344-025-0057-y
82. H.D. Liu, B. Tian, Y.Q. Chen, C.D. Cheng, X.T. Gao, N-soliton, Hth-order breather, hybrid and multi-pole solutions for a generalized variable-coefficient Gardner equation with an external force in a plasma or fluid. Nonlinear Dyn. **113**(4), 3655–3672 (2025). https://doi.org/10.1007/s11071-024-10397-1
83. H. Lemziouka, F. Nekkach, A. Boutahar, R. Moubah, L.H. Omari, M. Filali, A. Rjeb, H. Lassri, M. Abid, E.K. Hlil, M. El Yazidi, Effect of cobalt doping on the structural, linear, and nonlinear optical properties in $Ba_{1-x}Co_xTiO_3$ perovskites. J. Electron. Mater. **52**(5), 3420–3430 (2023). https://doi.org/10.1007/s11664-023-10311-2
84. X.Y. Gao, In an ocean or a river: bilinear auto-Bäcklund transformations and similarity reductions on an extended time-dependent (3+1)-dimensional shallow water wave equation. China Ocean Eng. **39**(1), 160–165 (2025). https://doi.org/10.1007/s13344-025-0012-y
85. X.Y. Gao, J.G. Liu, G.W. Wang, Inhomogeneity, magnetic auto-Bäcklund transformations and magnetic solitons for a generalized variable-coefficient Kraenkel-Manna-Merle system in a deformed ferrite. Appl. Math. Lett. **171**, 109615 (2025). https://doi.org/10.1016/j.aml.2025.109615
86. H. Benaali, S. Bahhar, A. Tahiri, Y. Didi, H. Fatihi, A. Abbassi, B. Manaut, M. Naji, Investigation of $KMnH_3$ and $KFeH_3$ perovskite hydrides via ab-initio for hydrogen storage. Inorg. Chem. Commun. (2024). https://doi.org/10.1016/j.inoche.2024.113033
87. M.A. Blanco, E. Francisco, V.G.I.B.B.S. Luana, GIBBS: isothermal-isobaric thermodynamics of solids from energy curves using a quasi-harmonic Debye model. Comput. Phys. Commun. **158**(1), 57–72 (2004). https://doi.org/10.1016/j.comphy.2003.12.001
88. A. Otero-De-La-Roza, D. Abbasi-Pérez, V. Luaña, Gibbs2: a new version of the quasiharmonic model code. II. Models for solid-state thermodynamics, features and implementation. Comput. Phys. Commun.

182(10), 2232–2248 (2011). https://doi.org/10.1016/j.cpc.2011.05.009
89. M.Z. Rana, M.R. Munshi, M. Al Masud, M.S. Zahan, Structural, electronic, optical and thermodynamic properties of $AlAuO_2$ and $AlAu_{094}Fe_{006}O_2$ compounds scrutinized by density functional theory (DFT). Heliyon (2023). https://doi.org/10.1016/j.heliyon.2023.e21405
90. A. Ayyaz, S. Saidi, N.D. Alkhaldi, G. Murtaza, N. Sfina, Q. Mahmood, Lead-free double perovskites Rb_2TlSbX_6 (X= Cl, Br, and I) as an emerging aspirant for solar cells and green energy applications. Sol. Energy **279**, 112844 (2024). https://doi.org/10.1016/j.solener.2024.112844
91. Z. Abbas, S.H. Mirza, A. Parveen, M. Aslam, S. Muhammad, Investigating the structural, electronic, optical and thermodynamic properties of $ATiO_3$ (A= Ba, Ca, Ra) for low-cost energy applications. Opt. Laser Technol. **181**, 111828 (2025). https://doi.org/10.1016/j.optlastec.2024.111828
92. M. Achqraoui, H. Jebari, N. Bekkioui, H. Ez-Zahraouy, Tensile effect on photocatalytic and optoelectronic properties of MoS_2 for hydrogen production: DFT study. Int. J. Hydrogen Energy **51**, 623–632 (2024). https://doi.org/10.1016/j.ijhydene.2023.10.152
93. M. Majji, S.M. Abzal, N. Jacob, P. Maiti, S. Choppella, M.K. Ravva, P.S. Maram, S. Ghosh, J.K. Dash, M. Motapothula, Efficient photocatalytic green hydrogen production using crystalline elemental Boron nanostructures under visible light. Int. J. Hydrog. Energy **56**, 338–347 (2024). https://doi.org/10.1016/j.ijhydene.2023.12.113
94. H. Bentour, M. Boujnah, M. Houmad, M. El Yadari, A. Benyoussef, A. El Kenz, DFT study of Se and Te doped $SrTiO_3$ for enhanced visible-light driven photocatalytic hydrogen production. Opt. Quant. Electron. **53**, 1–13 (2021). https://doi.org/10.1007/s11082-021-03214-1
95. H. Bentour, K. Belasfar, M. Boujnah, M. El Yadari, A. Benyoussef, A. El Kenz, DFT study of Se/Mn and Te/Mn codoped $SrTiO_3$ for visible light-driven photocatalytic hydrogen production. Opt. Mater. **129**, 112431 (2022). https://doi.org/10.1016/j.optmat.2022.112431
96. Y. Xu, M.A. Schoonen, The absolute energy positions of conduction and valence bands of selected semiconducting minerals. Am. Mineral. **85**(3–4), 543–556 (2000). https://doi.org/10.2138/am-2000-0416
97. L.J. Bartolotti. Absolute electronegativities as determined from Kohn-Sham theory. In Electronegativity (pp. 27–40). Berlin, Heidelberg: Springer Berlin Heidelberg. https://doi.org/10.1007/BFb0029835 (2005)
98. G.Z. Wang, H. Chen, X.K. Luo, H.K. Yuan, A.L. Kuang, Bandgap engineering of $SrTiO_3/NaTaO_3$ heterojunction for visible light photocatalysis. Int. J. Quantum Chem. **117**(20), e25424 (2017). https://doi.org/10.1002/qua.25424
99. N. Fajrina, M. Tahir, A critical review in strategies to improve photocatalytic water splitting towards hydrogen production. Int. J. Hydrogen Energy **44**(2), 540–577 (2019). https://doi.org/10.1016/j.ijhydene.2018.10.200
100. S. Hussain, J.U. Rehman, M.M. Shahid, M.U. Farooq, A. Hussain, M.B. Tahir, Study of inorganic perovskite RGaO3 (R = Rb and Na) oxide alloys for photocatalytic applications: a DFT insights. Phys. B Condens. Matter **695**, 416473 (2024). https://doi.org/10.1016/j.physb.2024.416473